An End-to-End DC-to-DC Efficiency Optimization and Design Analysis for MIMO Wireless Power Transfer Systems

Young-Seok Lee, *Graduate Student Member, IEEE*, Taeyeong Yoon, *Graduate Student Member, IEEE*, Jungsuek Oh, *Senior Member, IEEE*, and Sangwook Nam, *Life Senior Member, IEEE*

***Abstract*—This article presents an end-to-end DC-to-DC efficiency optimization framework for wireless power transfer (WPT) systems that jointly accounts for the nonlinear characteristics of both the power amplifier (PA) and the rectifier. Using measurement-based models—an affine function for the PA and a concave piecewise linear (PWL) function for the rectifier—the optimization is formulated as a semidefinite program (SDP) that directly maximizes the DC-to-DC efficiency under a transmit DC power budget constraint. When the SDP relaxation yields a higher rank solution that cannot be directly realized as a single beam, its objective value provides a reasonable upper bound on the achievable DC power; a successive convex approximation (SCA) procedure then recovers a feasible rank-one excitation vector, achieving a recovery ratio exceeding 97% across all tested conditions. Although the formulation is general and applicable to any array configuration, including SISO and MISO, it is validated on a multiple-input–multiple-output (MIMO) system where the near-field focusing effect is impactful. Three optimization frameworks—RF-to-RF, RF-to-DC, and DC-to-DC—are systematically compared. Simulation results using a 5.64-GHz system with a 12 $\times$ 12 transmit array and an 8 $\times$ 8 receive rectenna array show that the DC-to-DC optimization achieves 31% and 48% higher end-to-end efficiency than the RF-to-DC and RF-to-RF approaches, respectively, at a distance of 0.5 m. Experimental validation on a fabricated 16 $\times$ 16 TX array and a 5 $\times$ 5 rectenna confirms that the measured DC-to-DC efficiency closely follows the simulation across both distance and azimuth sweeps.**

***Index Terms*—DC-to-DC efficiency, multiple-input–multiple-output (MIMO), rectenna, semidefinite programming, wireless power transfer (WPT).**

I. Introduction

WIRELESS power transfer (WPT) technology has been extensively studied over the past decades, motivated by the growing demand for cable-free power delivery to electronic devices [1], [2], [3], [4]. WPT can be broadly classified into three major categories. Inductive WPT has been successfully commercialized in mobile devices under the Qi standard [5], [6]. Resonant WPT, demonstrated by Kurs et al. [7] through strongly coupled magnetic resonances, extends the effective range to mid-field distances and is being adopted in electric vehicle (EV) charging applications. RF-based WPT, pioneered by Brown [8] through microwave beam transmission experiments, can deliver power over the longest distances among the three categories by directly radiating electromagnetic energy [9]. Notably, this concept traces back to the original vision of Nikola Tesla, who first proposed the idea of wireless energy transfer [10].

However, compared with inductive and resonant WPT, RF-based WPT (hereafter referred to simply as WPT) suffers from inherently low system-level efficiency. In the propagation domain, the transmitted power spreads over distance, fundamentally limiting the energy captured by the receiver [14]. In the circuit domain, the power amplifier (PA) on the transmit side and the rectifier on the receive side each introduce nonlinear losses that further degrade the overall efficiency. These multistage losses together form a major bottleneck for practical WPT systems. Consequently, optimizing the *transmit excitation* at the transmitter array (TXA) to maximize the end-to-end efficiency is of critical importance.

Numerous studies have investigated WPT efficiency optimization in the RF domain. RF-to-RF efficiency, commonly referred to as power transfer efficiency (PTE) [15], [16] or beam collection efficiency (BCE) [17], [18], is hereinafter denoted as PTE in this article. Enhancing PTE has been studied through a variety of approaches [19], [20], [21], [22], [23], [24], [25], [26]. In the context of planar arrays, Oliveri et al. [19] formulated the PTE maximization as a generalized eigenvalue problem and obtained the optimal array weights in closed form. Zhang and Ho [27] further introduced a convex optimization framework for multiple-input–multiple-output (MIMO) systems, casting the energy beamforming problem as a semidefinite program (SDP) and showing that the optimal transmit covariance matrix admits a rank-one solution under a sum-(RF) power constraint. PTE has long served as a primary figure of merit (FoM) for characterizing WPT system performance due to its mathematical tractability and physical clarity. However, PTE alone cannot capture the behavior of the entire WPT system, as it entirely neglects the DC-domain losses introduced by the PA and rectifier.

Received 25 April 2026; revised 1 June 2026 and 29 June 2026; accepted 15 July 2026. This work was supported by the Institute of Information and Communications Technology Planning and Evaluation (IITP) grant funded by Korean Government (MSIT) (Advanced and Integrated Software Development for Electromagnetic Analysis) under Grant 2019-II190098. *(Corresponding author: Sangwook Nam.)*

The authors are with the Institute of New Media and Communication (INMC) and the Department of Electrical and Computer Engineering (ECE), Seoul National University, Seoul 08826, Republic of Korea (e-mail: ryanlee@snu.ac.kr; taeyeong.yoon@snu.ac.kr; jungsuek@snu.ac.kr; snam@snu.ac.kr).

Digital Object Identifier 10.1109/TMTT.2026.3714844

TABLE I
COMPARISON OF END-TO-END WPT OPTIMIZATION FRAMEWORKS

Ref.	TX–RX	Signal	PA model	Rectifier model	Optimization	RX power	Exp.
[11]	SISO	Multi-tone	Rapp (analytical)	Taylor 4th-order	SCP + SQP	μW	No
[12]	MISO (DMA)	Multi-tone	Linear	Taylor 4th-order	AO + SCA	μW	No
[13]	MISO (hybrid)	Multi-tone	Rapp (analytical)	Diode eq. (Lambert W)	PSO / DDPG	μW	No
This work	**MIMO**	**CW**	**Meas.-based affine**	**Meas.-based PWL**	**SDP + SCA**	**mW–W**	**Yes**

To address this limitation, several studies have explored RF-to-DC efficiency by incorporating the rectifier's nonlinear power conversion behavior. Wan and Huang [28] first introduced the concept of "transmission-conversion efficiency (TCE)," defined as the product of PTE and the rectifier's power conversion efficiency (PCE), and showed that optimizing the aperture magnitude distribution of the transmitting antenna can improve TCE compared with uniform excitation. Sun et al. [29] proposed an optimization strategy under nonuniform incident power density distribution, where the load resistance of each rectifier is individually optimized to maximize the total PCE of the rectenna array. However, these works addressed PTE and PCE improvements separately rather than jointly optimizing the transmit excitation vector to maximize TCE as a *unified metric*. Shen and Clerckx [30] took a step further by formulating a joint beamforming optimization that directly maximizes TCE. However, their rectifier model is based on a Taylor-series approximation of the diode current equation, which is only valid in the linear (small-signal) operating region and does not account for saturation effects at higher power levels. Subsequently, Lee et al. [31] proposed a TCE maximization framework that employs a measurement-based rectifier model, capturing the full nonlinear PCE characteristics including saturation. Despite these advances, all RF-to-DC approaches still do not account for PA nonlinearity on the transmit side.

In a practical WPT system, power is supplied in DC form at the transmitter and ultimately delivered as DC power to the load at the receiver. Therefore, DC-to-DC efficiency represents the major end-to-end FoM for WPT systems. Despite its importance, DC-to-DC efficiency has only recently been treated as an explicit optimization objective. Some earlier works computed the overall efficiency by simple stagewise multiplication: the product of PTE and PCE has been used to evaluate RF-to-DC efficiency [32], while DC-to-DC efficiency has been reported by further including the PA efficiency as an additional multiplicative factor [1], [33]. Jiang et al. [34] explicitly defined DC-to-DC efficiency as part of a system-level FoM and optimized it with respect to design parameters such as operating frequency and antenna aperture area, though their optimization target was cost-efficient system architecture rather than the transmit excitation vector.

More recently, end-to-end optimization frameworks that jointly account for PA and rectifier nonlinearities have emerged, primarily in the context of multitone waveform design. Zhang and Clerckx [11] addressed the fundamental tradeoff between PA and energy harvester nonlinearities, showing that high-PAPR waveforms favored by the rectifier conflict

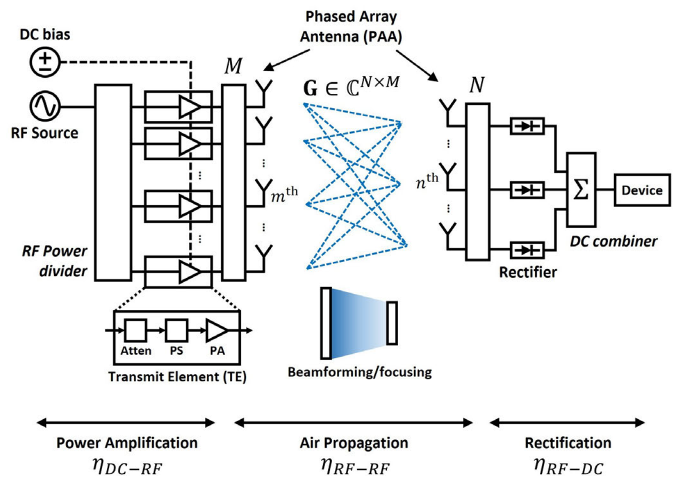

Fig. 1. Block diagram of the MIMO WPT system considered in this work. The end-to-end power flow consists of three stages: PA ($\eta_{\mathrm{DC-RF}}$), free-space channel ($\eta_{\mathrm{RF-RF}}$), and rectifier ($\eta_{\mathrm{RF-DC}}$).

with the PA's preference for low-PAPR signals; however, their formulation is restricted to a SISO link with an analytical Rapp PA model and a Taylor-expansion rectifier model. Azarbahram et al. [12] extended waveform optimization to a multiantenna transmitter with dynamic metasurface antennas, but assumed linear PA operation and modeled only the rectifier nonlinearity. Khattak et al. [13], [35] proposed a joint waveform and hybrid beamforming design incorporating both the Rapp PA model and a diode-equation-based rectifier model; however, the solution was obtained through heuristic optimization, and the optimality gap was not explicitly quantified. As summarized in Table I, these works share several common characteristics: multitone waveform optimization in SISO or MISO configurations, analytical device models valid over a limited operating range, and no experimental validation. These aspects leave a gap for practical phased-array WPT systems, where continuous wave (CW) operation is practical, and the PA and rectifier behavior must be characterized across the full operating range.

This article addresses this gap by proposing a *DC-to-DC efficiency optimization framework for practical CW-based MIMO WPT systems* that encompasses all three power conversion stages: PA, free-space propagation channel, and rectifier. The proposed framework targets a different design domain from the multitone waveform approaches in [11], [12], and [13]: it directly optimizes the CW excitation vector of a phased-array transmitter, which is the prevailing architecture in practical WPT deployments. Rather than relying on analytical

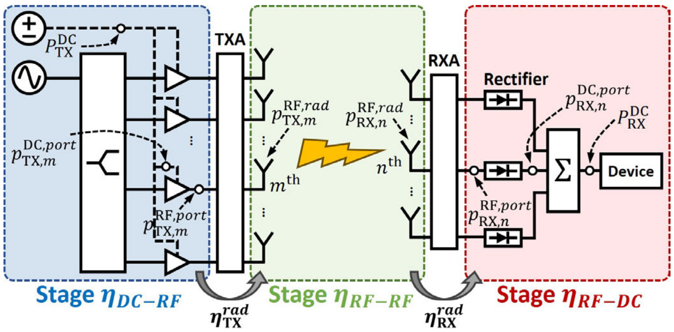

Fig. 2. Detailed power flow and per-element variables across the three stages. Superscripts "port" and "rad" distinguish antenna port-level and radiated quantities, respectively. Lowercase variables (p) denote per-element quantities, and uppercase variables (P) denote system-level totals.

device equations, the PA and rectifier behaviors are captured through measurement-based piecewise linear (PWL) models derived from hardware characterization, enabling accurate representation of device behavior across the full operating range, including saturation. The resulting optimization is cast as an SDP via SDR [36], and a successive convex approximation (SCA) procedure [37] is developed to recover a feasible rank-one excitation vector from the relaxed solution. By providing both an efficiency upper bound and a feasible excitation vector for any given hardware configuration, this framework serves as a practical tool for RF engineers to evaluate achievable system-level performance and to determine the optimal transmit excitation for maximum DC power delivery. The main contributions are as follows.

1) A DC-to-DC optimization framework for MIMO WPT systems that jointly accounts for PA and rectifier nonlinearities through measurement-based models capturing the device characteristics across the operating range.
2) An SDP-based formulation that provides both an upper bound on the achievable DC-to-DC efficiency for a given system configuration and a high-quality feasible excitation through SCA-based rank-one recovery.
3) A systematic comparative analysis of three optimization strategies—RF-to-RF (PTE), RF-to-DC (TCE), and DC-to-DC—under consistent conditions across diverse scenarios, quantifying how PA and rectifier nonlinear coupling affects the optimal excitation design.
4) Experimental validation using a TXA and rectenna prototype, demonstrating the accuracy of the DC-to-DC framework under real-world operating conditions.

The TXA hardware used in this work was fabricated and calibrated in our prior work [38], [39], [40]. Preliminary results of this study were first presented in [41].

The remainder of this article is organized as follows. Section II describes the MIMO WPT system model and defines the efficiency metrics. Section III presents the three optimization frameworks: RF-to-RF (PTE), RF-to-DC (TCE), and the proposed DC-to-DC, along with the SCA-based rank-one recovery procedure. Section IV provides simulation results and comparative analysis across multiple scenarios. Section V presents experimental validation through measurements. Section VI discusses the modeling scope and projects the performance with state-of-the-art devices. Finally, Section VII concludes this article.

II. Background

A. System Model

Fig. 1 illustrates the MIMO WPT system considered in this work. The transmitter side consists of a TXA with M antenna elements. A common RF source feeds all transmit paths via a power divider, and each path forms a transmit element (TE) comprising an attenuator, a phase shifter (PS), and a PA in cascade, enabling independent control of the magnitude and phase at each element.[1] The receiver side consists of a receiver array (RXA) with N rectifying elements, where each element rectifies the incoming RF power independently. The DC outputs from all rectifiers are then combined through a DC combiner to deliver the total DC power to the load.

The end-to-end power flow from the DC supply to the load traverses three distinct stages, as indicated in Fig. 1.

1) *Power Amplification Stage ($\eta_{\mathrm{DC-RF}}$):* Each PA consumes DC power to amplify the RF signal. Due to the nonlinear input–output characteristics of practical PAs, the efficiency varies with the operating power level.
2) *Air Propagation Stage ($\eta_{\mathrm{RF-RF}}$):* The RF signals radiated by the TXA propagate through free space and are captured by the RXA. The received power at each RXA element depends on the transmit excitation, the array geometry, and the propagation environment.
3) *Rectification Stage ($\eta_{\mathrm{RF-DC}}$):* Each rectifier converts the received RF power into DC power. Like the PA, the rectifier exhibits nonlinear conversion characteristics that depend on the input power level.

The following assumptions are adopted across this article.

1) Free-space propagation is assumed for the channel.
2) All PAs and all rectifiers are assumed to have identical nonlinear characteristics, modeled based on measurement data as detailed in Section III.
3) DC power combining at the RXA is ideal, i.e., the total received DC power equals the arithmetic sum of the individual rectifier outputs.[2]

B. System Efficiency Metrics

Throughout this article, the three system-level efficiencies are referred to as "RF-to-RF," "RF-to-DC," and "DC-to-DC." For brevity, these terms are abbreviated as "RF–RF," "RF–DC," and "DC–DC," respectively, in this article title, figure captions, table entries, and subscripts.

Figs. 2 and 3 detail the power flow variables and efficiency metric definitions at each stage. At the transmitter, the mth PA consumes DC power $p_{\mathrm{TX},m}^{\mathrm{DC},port}$ and delivers RF output power

[1]Most of the WPT systems omit the attenuator and transmit at full power with phase-only control to reduce hardware complexity, and also to achieve higher power at the receiver. The architecture shown here represents the general case where both magnitude and phase are adjustable, since magnitude tapering significantly affects the system efficiency.

[2]The design of practical DC combining or mathematical modeling of the combining framework is beyond the scope of this article.

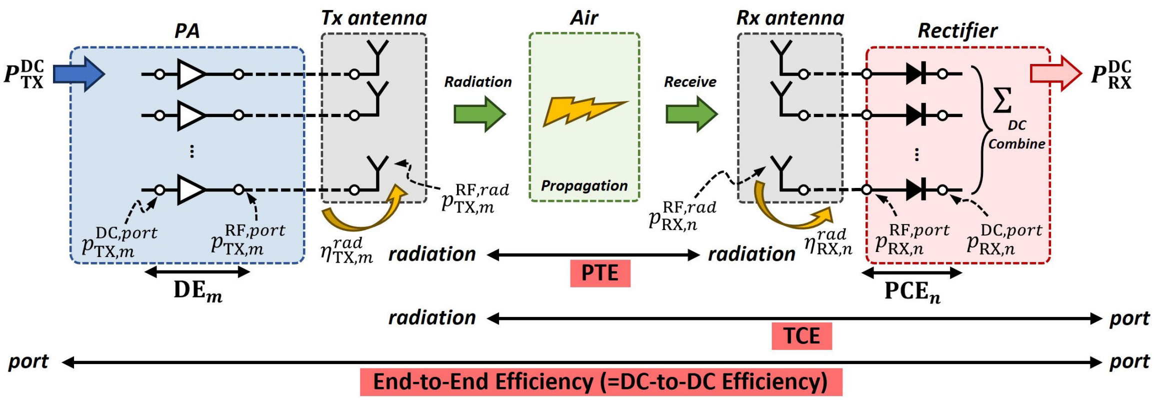

Fig. 3. System-level power flow and efficiency metric definitions. DE_m, PTE, PCE_n, TCE, and end-to-end efficiency span progressively broader portions of the power chain. The radiation efficiencies $\eta_{\mathrm{TX},m}^{\mathrm{rad}}$ and $\eta_{\mathrm{RX},n}^{\mathrm{rad}}$ bridge the port-level and radiated quantities.

$p_{\mathrm{TX},m}^{\mathrm{RF},port}$ at the antenna port. The drain efficiency (DE) of the mth PA is defined as

$$\mathrm{DE}_m = \frac{p_{\mathrm{TX},m}^{\mathrm{RF},port}}{p_{\mathrm{TX},m}^{\mathrm{DC},port}}. \tag{1}$$

At the receiver, the nth rectifier receives RF power $p_{\mathrm{RX},n}^{\mathrm{RF},port}$ at its input port and produces DC output power $p_{\mathrm{RX},n}^{\mathrm{DC},port}$. The PCE of the nth rectifier is

$$\mathrm{PCE}_n = \frac{p_{\mathrm{RX},n}^{\mathrm{DC},port}}{p_{\mathrm{RX},n}^{\mathrm{RF},port}}. \tag{2}$$

The system-level power quantities are obtained by summing over all elements

$$P_{\mathrm{TX}}^{\mathrm{DC}} = \sum_{m=1}^{M} p_{\mathrm{TX},m}^{\mathrm{DC},port}, \quad P_{\mathrm{TX}}^{\mathrm{RF},port} = \sum_{m=1}^{M} p_{\mathrm{TX},m}^{\mathrm{RF},port} \tag{3}$$

$$P_{\mathrm{RX}}^{\mathrm{RF},port} = \sum_{n=1}^{N} p_{\mathrm{RX},n}^{\mathrm{RF},port}, \quad P_{\mathrm{RX}}^{\mathrm{DC}} = \sum_{n=1}^{N} p_{\mathrm{RX},n}^{\mathrm{DC},port} \tag{4}$$

where $P_{\mathrm{TX}}^{\mathrm{RF},port}$ and $P_{\mathrm{RX}}^{\mathrm{RF},port}$ denote the total RF power at the transmit and receive antenna ports, respectively.

The end-to-end DC-to-DC efficiency is defined as

$$\eta_{\mathrm{DC-DC}} = \frac{P_{\mathrm{RX}}^{\mathrm{DC}}}{P_{\mathrm{TX}}^{\mathrm{DC}}}. \tag{5}$$

To decompose $\eta_{\mathrm{DC-DC}}$ into physically meaningful stages, the antenna radiation efficiency must be accounted for, as indicated in Fig. 2. Let $\eta_{\mathrm{TX},m}^{\mathrm{rad}}$ and $\eta_{\mathrm{RX},n}^{\mathrm{rad}}$ be the radiation efficiency of the mth transmit and nth receive antenna element, respectively. The per-element radiated power from the mth transmit antenna and the per-element power incident on the nth receive antenna (before the antenna loss) are

$$p_{\mathrm{TX},m}^{\mathrm{RF,rad}} = \eta_{\mathrm{TX},m}^{\mathrm{rad}} \cdot p_{\mathrm{TX},m}^{\mathrm{RF},port}, \quad p_{\mathrm{RX},n}^{\mathrm{RF,rad}} = \frac{p_{\mathrm{RX},n}^{\mathrm{RF},port}}{\eta_{\mathrm{RX},n}^{\mathrm{rad}}} \tag{6}$$

and the corresponding system-level totals are

$$P_{\mathrm{TX}}^{\mathrm{RF,rad}} = \sum_{m=1}^{M} \eta_{\mathrm{TX},m}^{\mathrm{rad}} \cdot p_{\mathrm{TX},m}^{\mathrm{RF},port} \tag{7}$$

$$P_{\mathrm{RX}}^{\mathrm{RF,rad}} = \sum_{n=1}^{N} \frac{p_{\mathrm{RX},n}^{\mathrm{RF},port}}{\eta_{\mathrm{RX},n}^{\mathrm{rad}}}. \tag{8}$$

PTE is then defined as the radiated-to-radiated efficiency

$$\eta_{\mathrm{RF-RF}}\ (\mathrm{PTE}) = \frac{P_{\mathrm{RX}}^{\mathrm{RF,rad}}}{P_{\mathrm{TX}}^{\mathrm{RF,rad}}} \tag{9}$$

which is equivalent to the BCE defined in [18], [19], and [40], quantifying the fraction of total radiated power collected at the receiver aperture.

Using these definitions, the end-to-end efficiency is expressed as $\eta_{\mathrm{DC-DC}} = P_{\mathrm{RX}}^{\mathrm{DC}}/P_{\mathrm{TX}}^{\mathrm{DC}}$, where $\eta_{\mathrm{DC-RF}} = P_{\mathrm{TX}}^{\mathrm{RF},port}/P_{\mathrm{TX}}^{\mathrm{DC}}$ is the system-level PA efficiency and $\eta_{\mathrm{RF-DC}} = P_{\mathrm{RX}}^{\mathrm{DC}}/P_{\mathrm{RX}}^{\mathrm{RF},port}$ is the system-level rectifier efficiency, as labeled in Fig. 2. When all antenna elements are identical, i.e., $\eta_{\mathrm{TX},m}^{\mathrm{rad}} = \eta_{\mathrm{TX}}^{\mathrm{rad}}$ for all m and $\eta_{\mathrm{RX},n}^{\mathrm{rad}} = \eta_{\mathrm{RX}}^{\mathrm{rad}}$ for all n, this simplifies to the cascade form

$$\eta_{\mathrm{DC-DC}} = \underbrace{\eta_{\mathrm{DC-RF}}}_{\mathrm{PA}} \cdot \eta_{\mathrm{TX}}^{\mathrm{rad}} \cdot \underbrace{\eta_{\mathrm{RF-RF}}}_{\text{Air propagation}} \cdot \eta_{\mathrm{RX}}^{\mathrm{rad}} \cdot \underbrace{\eta_{\mathrm{RF-DC}}}_{\text{Rectifier}} \tag{10}$$

where $\eta_{\mathrm{TX}}^{\mathrm{rad}}$ and $\eta_{\mathrm{RX}}^{\mathrm{rad}}$ become fixed constants independent of the excitation, whereas the three stage efficiencies $\eta_{\mathrm{DC-RF}}$, $\eta_{\mathrm{RF-RF}}$, and $\eta_{\mathrm{RF-DC}}$ vary with the operating conditions.

While (10) provides a clean decomposition, optimizing each stage independently is suboptimal due to the nonlinear coupling between them. The PA excitation determines the transmit beam pattern, governing PTE, and simultaneously shapes the received power distribution across the rectifier array, governing the per-element PCE. This interstage coupling motivates the direct optimization of $\eta_{\mathrm{DC-DC}}$ formulated in Section III.

III. Optimization Frameworks

This section formulates three optimization problems that correspond to progressively more comprehensive efficiency metrics: RF-to-RF (PTE), RF-to-DC (TCE), and DC-to-DC. Throughout this section, all antenna elements are assumed to be identical, so that $\eta_{\mathrm{TX},m}^{\mathrm{rad}} = \eta_{\mathrm{TX}}^{\mathrm{rad}}$ for all m and $\eta_{\mathrm{RX},n}^{\mathrm{rad}} = \eta_{\mathrm{RX}}^{\mathrm{rad}}$ for all n. Since these radiation efficiencies are then fixed constants independent of the transmit excitation, they do not influence the optimal solution and are omitted from the optimization formulations hereafter.

A. System Architecture and Channel Model

Let $G \in \mathbb{C}^{N\times M}$ be the channel matrix between the TXA and RXA, and let $x_t \in \mathbb{C}^{M\times 1}$ be the transmit excitation vector. The channel matrix $\mathbf{G}$ is computed from the free-space propagation model incorporating the antenna element patterns. The transmit covariance matrix is defined as $S = \mathbb{E}[x_t x_t^H] \succeq 0$. Using $\mathbf{S}$, the per-element transmit and receive RF powers at the antenna ports are expressed as

$$p_{\mathrm{TX},m}(S) = S_{mm}/Z \tag{11}$$

$$p_{\mathrm{RX},n}(S) = \mathrm{tr}(C_n S)/Z \tag{12}$$

where Z is the characteristic impedance and $C_n = G^H E_n G$, with $E_n \in \mathbb{R}^{N\times N}$ being the selection matrix whose only nonzero entry is $[E_n]_{nn} = 1$.

The rectifier and PA behaviors are modeled by measurement-based functions. The rectifier maps RF input power to DC output power through a concave PWL

$$p_{\mathrm{RX},n}^{\mathrm{DC},port} = f\left(p_{\mathrm{RX},n}^{\mathrm{RF},port}\right) = \min_{k\in\mathcal{K}}\left(a_k\, p_{\mathrm{RX},n}^{\mathrm{RF},port} + b_k\right) \tag{13}$$

where $\{(a_k, b_k)\}_{k\in\mathcal{K}}$ are the slopes and intercepts of the $|\mathcal{K}|$ segments. The concavity of $f(\cdot)$ reflects the decreasing PCE at high input power due to rectifier saturation. The PA maps RF output power to the DC consumption through an affine function

$$p_{\mathrm{TX},m}^{\mathrm{DC},port} = h\left(p_{\mathrm{TX},m}^{\mathrm{RF},port}\right) = \alpha\, p_{\mathrm{TX},m}^{\mathrm{RF},port} + \beta \tag{14}$$

where α and β are the slope and intercept obtained from measurement-based regression. Under the identical-element assumption, the same $f(\cdot)$ and $h(\cdot)$ apply to all rectifiers and PAs, respectively.

B. RF-to-RF Efficiency (PTE) Optimization

The PTE optimization maximizes the total received RF power for a given total transmit RF power. Since maximizing $P_{\mathrm{RX}}^{\mathrm{RF},rad}$ under fixed $P_{\mathrm{TX}}^{\mathrm{RF},rad}$ is equivalent to maximizing $\eta_{\mathrm{RF-RF}}$ (PTE), the problem is formulated as [40]

$$\max_{S}\ \mathrm{tr}\left(GSG^H\right)/Z \tag{15a}$$

$$\text{s.t. } \mathrm{tr}(S)/Z = P_t^{\mathrm{RF}} \tag{15b}$$

$$S \succeq 0 \tag{15c}$$

where P_t^{RF} is the total transmit RF power budget. The objective is linear in $\mathbf{S}$, making this a standard SDP with a globally optimal solution. The rank of the optimal S^* is guaranteed to be one for this formulation, and the optimal transmit vector is directly obtained as $x_t^* = (\lambda_1)^{1/2} v_1$ from the eigenvalue decomposition of S^*.

Equivalently, the PTE maximization also can be expressed as the Rayleigh quotient [19]:[3]

$$\eta_{\mathrm{RF-RF}} = \frac{x_t^H G^H G\, x_t}{x_t^H x_t} \tag{16}$$

whose maximum is attained by the dominant eigenvector of $G^H G$. This generalized eigenvalue formulation admits a closed-form solution and guarantees global optimality. The absence of PA and rectifier constraints makes this closed-form solution possible. When such nonlinear device constraints are introduced—as in the TCE and DC-to-DC formulations below—the problem no longer reduces to an eigenvalue problem, and finding the globally optimal excitation vector directly becomes intractable.

C. RF-to-DC Efficiency (TCE) Optimization

TCE optimization extends the scope of PTE optimization to include the rectifier behavior [31]. By incorporating the concave PWL rectifier model (13) into the PTE formulation, the problem becomes:[4]

$$\max_{S,t}\ \sum_{n=1}^{N} t_n \tag{17a}$$

$$\text{s.t. } \mathrm{tr}(S)/Z \le P_t^{\mathrm{RF}} \tag{17b}$$

$$S \succeq 0 \tag{17c}$$

$$t_n \le a_k\, p_{\mathrm{RX},n}(S) + b_k \quad \forall n \quad \forall k\in\mathcal{K} \tag{17d}$$

$$p_{\mathrm{RX},n}^{\min} \le p_{\mathrm{RX},n}(S) \le p_{\mathrm{RX},n}^{\max} \quad \forall n \tag{17e}$$

where t_n is an auxiliary variable representing the DC output of the nth rectifier, upper bounded by the PWL approximation of $f(\cdot)$ through the hypograph constraints. The input power range $[p_{\mathrm{RX},n}^{\min}, p_{\mathrm{RX},n}^{\max}]$ enforces valid rectifier operating conditions. Since $f(\cdot)$ is concave, the hypograph constraints are linear in $\mathbf{S}$ and $\mathbf{t}$, preserving the SDP structure. Note that the power constraint (17b) uses an inequality rather than the equality in (15b): unlike PTE, where using the full power budget is always optimal, the TCE optimizer may benefit from transmitting less than P_t^{RF} to avoid driving rectifiers into saturation.

D. DC-to-DC Efficiency Optimization

1) Problem Formulation: The DC-to-DC formulation incorporates both the PA and rectifier nonlinearities, jointly optimizing the transmit excitation under a DC power budget

$$\max_{S,t}\ \sum_{n=1}^{N} t_n \tag{18a}$$

$$\text{s.t } \frac{\alpha}{Z}\mathrm{tr}(S) + M\beta \le P_t^{\mathrm{DC}} \tag{18b}$$

$$S \succeq 0 \tag{18c}$$

$$t_n \le a_k\, p_{\mathrm{RX},n}(S) + b_k \quad \forall n \quad \forall k\in\mathcal{K} \tag{18d}$$

$$p_{\mathrm{RX},n}^{\min} \le p_{\mathrm{RX},n}(S) \le p_{\mathrm{RX},n}^{\max} \quad \forall n \tag{18e}$$

$$p_{\mathrm{TX},m}^{\min} \le p_{\mathrm{TX},m}(S) \le p_{\mathrm{TX},m}^{\max} \quad \forall m \tag{18f}$$

[3]Since the channel matrix $\mathbf{G}$ is constructed from the realized gain, which embeds the antenna radiation efficiency, the ratio in (16) corresponds to the port-to-port power ratio rather than the radiated-to-radiated PTE. However, the two differ only by the constant factor $\eta_{\mathrm{TX}}^{\mathrm{rad}} \cdot \eta_{\mathrm{RX}}^{\mathrm{rad}}$, so the optimal excitation vector is identical.

[4]In [31], TCE optimization was solved via mixed-integer nonlinear programming (MINLP) to handle a general piecewise rectifier model. Since the rectifier model adopted in this article is restricted to concave PWL segments, the problem can be reformulated as an SDP with equivalent results. The additional rectifier constraints, however, do not guarantee a rank-one S^*; when the rank exceeds one, the same SCA-based rank-one recovery in Section III-D is applied. In practice, the rank remains low (typically ≤ 2).

where P_t^{DC} is the total DC power budget. The output power range $[p_{\mathrm{TX},m}^{\min}, p_{\mathrm{TX},m}^{\max}]$ enforces the valid RF output-power operating range of mth PA. The key difference from the TCE formulation (17) is the incorporation of the PA characteristic: the power budget is imposed on the P_t^{DC} rather than on the RF output. Since $h(\cdot)$ is affine, the total PA DC consumption $\sum_{m=1}^{M} h(p_{\mathrm{TX},m}) = (\alpha/Z)\mathrm{tr}(S) + M\beta$ reduces to a single linear constraint on $\mathbf{S}$, preserving the SDP structure without requiring auxiliary variables.

Since all constraints are linear in $\mathbf{S}$ and $\mathbf{t}$, this formulation is an SDP that can be solved globally using standard convex optimization tools. The globally optimal S^* may have rank greater than one and therefore does not directly correspond to a single transmit excitation vector. Nevertheless, its objective value $\bar{P}_{\mathrm{DC}} = \sum_{n=1}^{N} t_n^*$ represents the maximum total received DC power under the relaxed-rank constraint, providing an upper bound that no feasible single-beam solution can exceed.

2) Rank-One Recovery via SCA: Since a practical CW transmitter requires a single excitation vector x_t, a rank-one solution must be recovered from S^* when its rank exceeds one. The upper bound $\bar{P}_{\mathrm{DC}}$ established above certifies the quality of any recovered solution: $\sum_{n=1}^{N} f(p_{\mathrm{RX},n}(x_t)) \leq \bar{P}_{\mathrm{DC}}$ for all feasible x_t.

A rank-r solution $S^* = \sum_{i=1}^{r} \lambda_i v_i v_i^H$ can be interpreted as a time-sharing of r beams, where each eigenmode v_i would be transmitted for a fraction of time proportional to λ_i. These eigenmodes are jointly optimal under this relaxed-rank (time-division) assumption, but they do not necessarily span the best single-beam solution. Restricting the search to $x_t = \sum_{i=1}^{K} c_i v_i$ confines the optimization to a K-dimensional subspace of $\mathbb{C}^M$ dictated by the time-division-optimal modes, potentially missing single-beam solutions that better exploit the hardware constraints. Since the optimal single-beam excitation is not guaranteed to lie in this subspace, we formulate the rank-one recovery as a direct optimization over the full $\mathbb{C}^M$ space using SCA [37].

The rank-one problem is stated as

$$\max_{x_t \in \mathbb{C}^M} \sum_{n=1}^{N} f\left(p_{\mathrm{RX},n}(x_t)\right) \tag{19a}$$

$$\text{s.t. } p_{\mathrm{TX},m}^{\min} \leq p_{\mathrm{TX},m}(x_t) \leq p_{\mathrm{TX},m}^{\max} \quad \forall m \tag{19b}$$

$$0 \leq p_{\mathrm{RX},n}(x_t) \leq p_{\mathrm{RX},n}^{\max} \quad \forall n \tag{19c}$$

$$\frac{\alpha}{Z}\|x_t\|^2 + M\beta \leq P_t^{\mathrm{DC}} \tag{19d}$$

where $p_{\mathrm{TX},m}(x_t) = |x_{t,m}|^2/Z$ and $p_{\mathrm{RX},n}(x_t) = |g_n^H x_t|^2/Z$, with g_n^H denoting the nth row of $\mathbf{G}$. This problem is nonconvex because the objective involves a concave function $f(\cdot)$, composed with the convex quadratic $|g_n^H x_t|^2/Z$.

SCA resolves this nonconvexity by replacing the convex quadratic terms with affine lower bounds at each iteration. At the ith iteration with current point $x_t^{(i)}$, the received power $p_{\mathrm{RX},n}(x_t)$ is replaced by its first-order affine minorizer

$$\hat{q}_n\left(x_t; x_t^{(i)}\right) = \frac{2}{Z}\mathrm{Re}\left(\left(g_n^H x_t^{(i)}\right)^* g_n^H x_t\right) - \frac{\left|g_n^H x_t^{(i)}\right|^2}{Z} \tag{20}$$

which satisfies two properties: tangent point agreement, $\hat{q}_n(x_t^{(i)}; x_t^{(i)}) = p_{\mathrm{RX},n}(x_t^{(i)})$, and global lower bound, $\hat{q}_n(x_t; x_t^{(i)}) \leq p_{\mathrm{RX},n}(x_t)$ for all x_t. The derivation from the first-order convexity condition is provided in Appendix A. Since $f(\cdot)$ is concave and nondecreasing over the valid input range, and $\hat{q}_n$ is affine in x_t, the surrogate objective $\tilde{F}(x_t; x_t^{(i)}) = \sum_{n=1}^{N} f(\hat{q}_n(x_t; x_t^{(i)}))$ is concave. Maximizing this surrogate at each iteration yields the following second-order cone program (SOCP) subproblem:

Algorithm 1 SCA-SOCP Rank-One Recovery

Require: SDP solution $\mathbf{S}^*$, upper bound $\bar{P}_{\mathrm{dc}}$, tolerance ε
Ensure: Feasible transmit vector $\mathbf{x}_t^*$, recovery ratio ρ_{rec}
Compute EVD: $\mathbf{S}^* = \sum_i \lambda_i \mathbf{v}_i \mathbf{v}_i^H, \quad \lambda_1 \geq \lambda_2 \geq \cdots$
Initialize $\mathbf{x}_t^{(0)} \leftarrow \gamma\sqrt{\lambda_1}\mathbf{v}_1$ *(warm start)* ▷ *γ: feasibility scaling*
for $i = 0, 1, 2, \ldots$ **do**
  Compute $\hat{q}_n(\cdot\,; \mathbf{x}_t^{(i)})$ for all n via (20)
  Solve SOCP (21) $\rightarrow \mathbf{x}_t^{(i+1)}$
  Evaluate $F(\mathbf{x}_t^{(i+1)}) = \sum_n \max(f(p_{\mathrm{RX},n}(\mathbf{x}_t^{(i+1)})), 0)$
  if $|F(\mathbf{x}_t^{(i+1)}) - F(\mathbf{x}_t^{(i)})| < \varepsilon$ **then**
    break
  end if
end for
$\mathbf{x}_t^* \leftarrow \mathbf{x}_t^{(i+1)}$
$\rho_{\mathrm{rec}} \leftarrow F(\mathbf{x}_t^*)/\bar{P}_{\mathrm{dc}}$
return $\mathbf{x}_t^*$, ρ_{rec}

$$\max_{x_t,\, t} \sum_{n=1}^{N} t_n \tag{21a}$$

$$\text{s.t. } t_n \leq a_k\, \hat{q}_n\left(x_t; x_t^{(i)}\right) + b_k \quad \forall n \quad \forall k \in \mathcal{K} \tag{21b}$$

$$\hat{q}_n\left(x_t; x_t^{(i)}\right) \geq 0 \quad \forall n \tag{21c}$$

$$\left|g_n^H x_t\right| \leq \sqrt{p_{\mathrm{RX},n}^{\max} \cdot Z} \quad \forall n \tag{21d}$$

$$\left|x_{t,m}\right| \leq \sqrt{p_{\mathrm{TX},m}^{\max} \cdot Z} \quad \forall m \tag{21e}$$

$$\frac{\alpha}{Z}\|x_t\|^2 + M\beta \leq P_t^{\mathrm{DC}}. \tag{21f}$$

The first two sets of constraints are linear in x_t (since $\hat{q}_n$ is affine), while the remaining three are SOC constraints, confirming the SOCP structure. This subproblem is convex and can be solved to global optimality at each SCA iteration. In deriving (21), the lower PA output-power constraint $p_{\mathrm{TX},m}^{\min} \leq p_{\mathrm{TX},m}(x_t)$ in (19b) is relaxed because it is nonconvex in x_t, whereas the upper PA output-power constraint is convex and retained as (21e).

The SCA iterates $\{x_t^{(i)}\}$ produce a monotonically nondecreasing sequence of objective values, i.e., $F(x_t^{(i+1)}) \geq F(x_t^{(i)})$, where $F(x_t) = \sum_{n=1}^{N} f(p_{\mathrm{RX},n}(x_t))$. Since this sequence is bounded above by $\bar{P}_{\mathrm{DC}}$, convergence to a KKT stationary point of (19) is guaranteed (proof in Appendix B).

The SDP solution plays a dual role in this procedure: it provides the upper bound $\bar{P}_{\mathrm{DC}}$ for quality certification, and its dominant eigenvector $(\lambda_1)^{1/2} v_1$—scaled to satisfy the feasibility constraints—*serves as a warm start* for the SCA iterations, initiating the search from a direction that the relaxed optimization has already identified as favorable.

The quality of the recovered solution is measured by the new metric defined as the *recovery ratio*

$$\rho_{\mathrm{rec}} = \frac{P_{\mathrm{DC}}^*}{\bar{P}_{\mathrm{DC}}} \tag{22}$$

where $P^*_{\mathrm{DC}} = \sum_{n=1}^{N} \max(f(p_{\mathrm{RX},n}(x_t^*)), 0)$ is the total received DC power achieved by the final solution x_t^*, and the $\max(\cdot, 0)$ operator clamps the PWL model output to zero, since $f(\cdot)$ may return negative values at very low input powers as an artifact of the regression. A recovery ratio close to unity indicates that the SDP relaxation is tight and the recovered single-beam solution is near-optimal. The overall procedure is summarized in Algorithm 1.

IV. Simulation Results and Design Analysis

A. Simulation Setup

All simulations are performed in MATLAB on a desktop PC with an AMD Ryzen 7 5800X processor. The channel matrix $\mathbf{G}$ defined in Section III-A is constructed from the Friis free-space propagation model. The (n, m)th entry of $G \in \mathbb{C}^{N\times M}$, representing the channel from the mth TXA element to the nth RXA element, is expressed on a voltage scale as

$$G_{n,m} = |G_{n,m}|\, e^{j\angle G_{n,m}} \tag{23}$$

with the magnitude and phase given by

$$|G_{n,m}| = \frac{\lambda}{4\pi d_{n,m}} \sqrt{G_{\mathrm{TX}}\left(\theta_{\mathrm{TX},n,m}\right)\, G_{\mathrm{RX}}\left(\theta_{\mathrm{RX},n,m}\right)} \tag{24}$$

$$\angle G_{n,m} = \frac{2\pi}{\lambda} \cdot d_{n,m} = k \cdot d_{n,m} \tag{25}$$

where $d_{n,m}$ is the distance between the mth TXA element and the nth RXA element, $G_{\mathrm{TX}}(\theta)$ and $G_{\mathrm{RX}}(\theta)$ are the identical active element gain patterns of the TXA and RXA, respectively, and λ is the operating wavelength. The antenna radiation efficiency was $\eta_{\mathrm{rad}} = 86\%$. The antenna element design and characterization are detailed in [40]. Both the TXA and RXA are planar square arrays[5] ($M_t \times M_t$ and $N_r \times N_r$, respectively), where M_t and N_r are the number of elements along one side of each square array, with element spacing 0.6λ at the operating frequency of 5.64 GHz,[6] and $Z = 50\ \Omega$.

The rectifier and PA characteristics are captured by the measurement-based functions $f(\cdot)$ and $h(\cdot)$ defined in (13) and (14), respectively, and the same functions are used consistently throughout both the simulation analysis and experimental validation. The SDP problems (15)–(18) are solved using the CVX toolbox with the MOSEK solver for the RF–RF and DC–DC formulations and the SeDuMi solver for the RF–DC formulation. The SCA-SOCP rank-one recovery (Algorithm 1) is initialized with the dominant eigenvector of S^* and uses a convergence tolerance of $\varepsilon = 10^{-4}$.

The PA model $h(\cdot)$ is derived from measurements of the Skyworks SE5004L [42], a 5-GHz PA with a typical 1-dB compression point of 30–34 dBm. The same PA chip is used in the TXA TEs; however, since the on-board PA is not individually accessible for direct measurement, the characterization is performed using the manufacturer's evaluation board (SE5004L-EK1 EVB) [43], shown in Fig. 4. The EVB

[5]A square array is assumed only for simplicity. The framework itself is geometry-agnostic and applies to any (e.g., rectangular or nonuniform) array, as it depends solely on the resulting channel matrix $\mathbf{G}$.

[6]The operating frequency of 5.64 GHz was selected based on the measured array-level response of the fabricated 16×16 TXA [40], whose best matching response occurred near 5.64 GHz after full RF-chain integration.

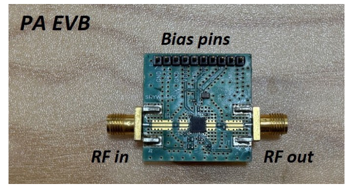

Fig. 4. Skyworks SE5004L-EK1 EVB used for PA characterization.

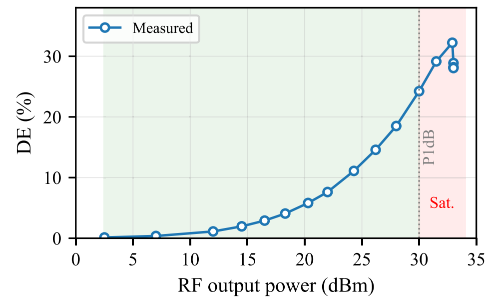

(a)

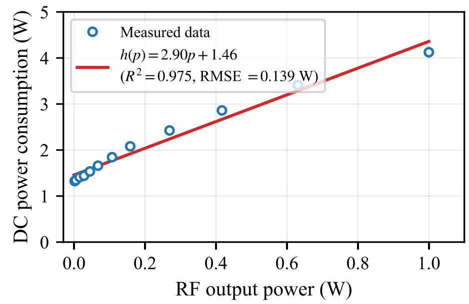

(b)

Fig. 5. PA characterization results. (a) Measured DE versus RF output power ($V_{\mathrm{CC}} = 5$ V). (b) DC power consumption versus RF output power. $h(p) = 2.90p + 1.46$ is fit via least-squares regression ($R^2 = 0.975$).

is biased at the rated supply voltage of $V_{\mathrm{CC}} = 5$ V. A CW signal is applied at the RF input, and for each input power level, the RF output power is recorded by spectrum analyzer while the DC power consumption is computed from the supply current measured at the EVB power supply ($P_{\mathrm{DC}} = V_{\mathrm{CC}} \times I_{\mathrm{CC}}$). Fig. 5(a) shows the measured DE across the full operating range.

The DE increases monotonically up to a peak of 32.2% near the compression point ($P_{\mathrm{out}} \approx 33$ dBm), beyond which the PA enters saturation, and the DE decreases. The PA characteristic is fit by a single affine function over the range $P_{\mathrm{out}} = 2.5$–30 dBm (2 mW–1 W), corresponding to the linear region below the compression point. The saturation region is excluded because the RF output power compresses while the DC consumption continues to increase, offering no benefit to the optimizer. Over the fitting range, the measured DC consumption exhibits a nearly affine relationship with the RF output power, as shown in Fig. 5(b). Although a slight concavity is observed at low power levels (a typical characteristic of class-AB bias), the affine regression achieves $R^2 = 0.975$ and RMSE = 0.14 W over the full fitting range. The relative error reaches approximately 10% at the lowest power level (2 mW) but decreases rapidly with increasing power. Since the affine model overestimates the DC consumption in this region,

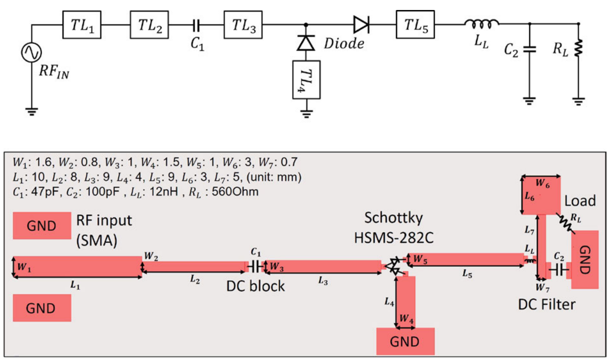

Fig. 6. Half-wave rectifier circuit: schematic (top) and layout (bottom).

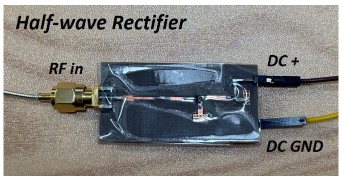

Fig. 7. Fabricated half-wave rectifier for 5.64 GHz.

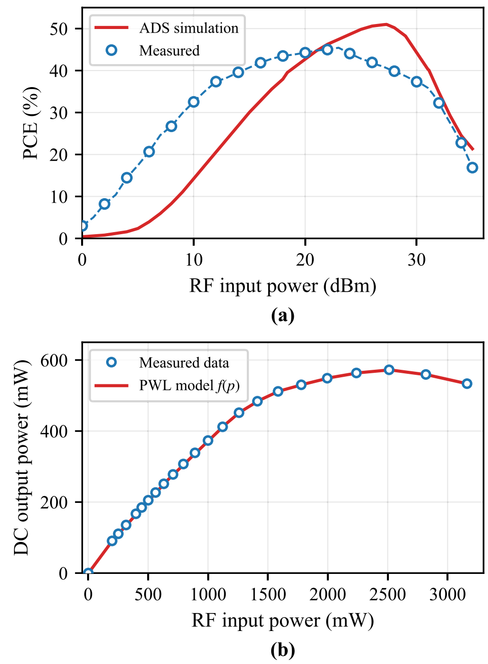

Fig. 8. Rectifier characterization results. (a) PCE versus RF input power: simulation and measurement. (b) DC output power versus RF input power. The concave PWL model $f(p)$ is fit over the range 0–35 dBm.

the resulting $\eta_{\text{DC-DC}}$ is a conservative estimate. The affine structure is specific to the class-AB PA used herein; other architectures (e.g., Doherty) would require recharacterization, though the framework remains applicable provided the PA model preserves convexity. The fit model is

$$h(p) = 2.90\,p + 1.46 \quad [\text{W}]. \tag{26}$$

This affine PA model simplifies the DC-to-DC SDP formulation in (18), where the total PA DC consumption reduces to a single linear constraint on $\mathbf{S}$.

The rectifier model $f(\cdot)$ is based on a simple half-wave rectifier designed and fabricated in-house for 5.64 GHz operation. Fig. 6 shows the circuit schematic and layout. The rectifier employs a Schottky diode (Avago HSMS-282C) with a microstrip matching network on a Taconic TLY-5A substrate (20 mil). The DC output filter consists of an inductor $L_L = 12$ nH and a capacitor $C_2 = 100$ pF, and the load resistance is optimized to $R_L = 560\ \Omega$. The circuit is designed using Keysight ADS, targeting a peak PCE of approximately 51% at the design frequency. Fig. 7 shows the fabricated rectifier.

The rectifier PCE is characterized by sweeping the RF input power from a signal generator and measuring the DC output voltage across R_L, from which the DC output power is computed as $P_{\text{DC}} = V_{\text{DC}}^2/R_L$. Fig. 8(a) compares the ADS simulation and measured PCE. The measured peak PCE is 45.4% at an input power of 23 dBm.

The measured DC output power versus RF input power characteristic is shown in Fig. 8(b). A concave PWL function $f(\cdot)$ is fit over the range 0–35 dBm (1–3162 mW), where the slopes remain monotonically decreasing, confirming the concavity required by the SDP formulation in (18). In the low-power linear region (the first segment), a linear regression is applied; in the higher power concave region, each segment directly connects consecutive measured data points without regression, enhancing the accuracy of the model. The complete segment parameters $\{(a_k, b_k)\}$ are listed in Table V

TABLE II
SUMMARY OF KEY MODEL PARAMETERS AND OPERATING CONSTRAINTS

Symbol	Description	Value
$h(\cdot)$	PA DC-consumption model	$h(p) = \alpha p + \beta$ W
α	PA model slope	2.90
β	PA model intercept	1.46 W
$f(\cdot)$	Rectifier DC-output model	12-segment PWL (Table V)
$p_{\text{TX},m}^{\max}$	PA output limit	1 W (30 dBm)
$p_{\text{RX},n}^{\max}$	Rectifier input limit	3162 mW (35 dBm)
$P_{\text{rect,peak}}$	Rectifier peak DC output	572 mW

(see Appendix C). The key model parameters and operating constraints used throughout the simulation and experiment are summarized in Table II. The same ranges over which $h(\cdot)$ and $f(\cdot)$ are characterized are imposed as the operating constraints $p_{\text{TX},m}^{\max}$ and $p_{\text{RX},n}^{\max}$ in (18), so the device models and their valid ranges are identical across the simulation and experiment.

Three simulation scenarios are considered. In Scenario 1, the TXA and RXA sizes are swept jointly at a fixed distance to analyze the tradeoff between array size and end-to-end efficiency and to identify a suitable array size pair for the subsequent analyses. Scenario 2 uses the array configuration determined in Scenario 1 and evaluates the three optimization frameworks (RF-to-RF, RF-to-DC, and DC-to-DC) over varying propagation conditions, including distance and angular displacement. Scenario 3 fixes the propagation geometry and sweeps the DC power budget P_t^{DC} to examine how each framework responds to different transmit power levels. In all three scenarios, the same set of PA and rectifier PWL models is applied, and the results are compared in terms of both the $\eta_{\text{DC-DC}}$ and the total received DC power $P_{\text{RX}}^{\text{DC}}$.

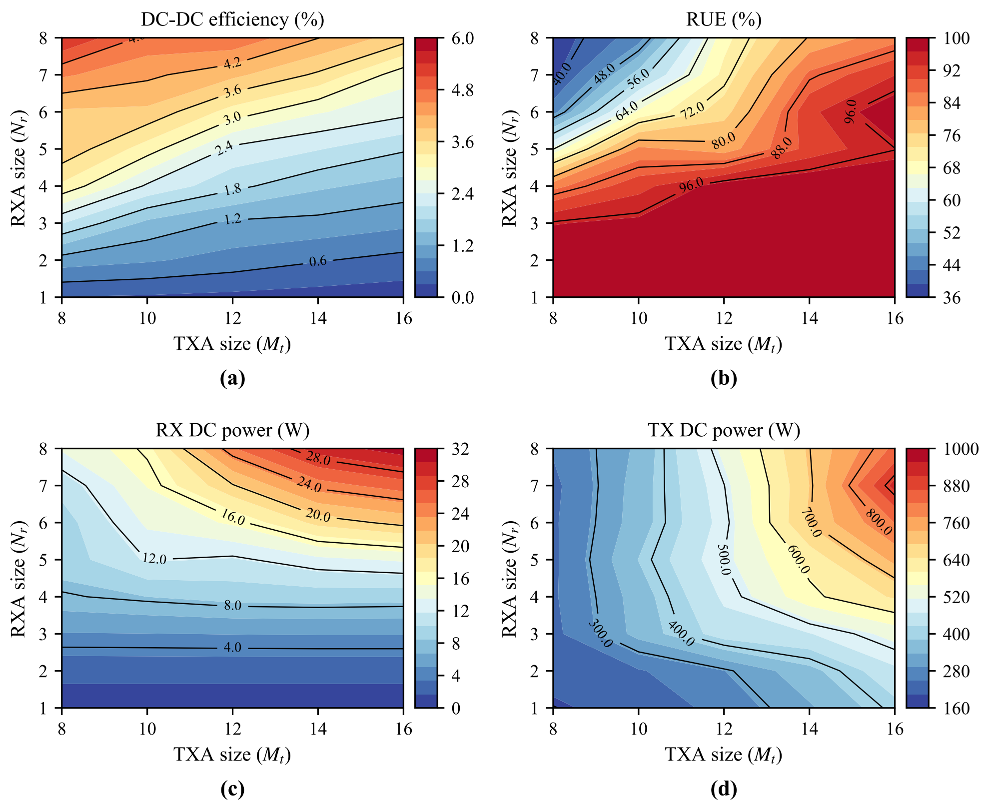

Fig. 9. Contour maps of (a) DC–DC efficiency, (b) RUE, (c) received DC power, and (d) TX DC power. d = 0.5 m with P_t^{DC} = 1200 W.

B. Array Size Tradeoff Analysis

The proposed DC-to-DC optimization framework provides a system-level design tool for MIMO WPT, where the TXA and RXA sizes are fundamental design parameters that govern the tradeoff among efficiency, received power, and rectifier utilization. This section investigates these tradeoffs by sweeping the array sizes and identifies a suitable TXA–RXA pair for the analyses in Sections IV-C and IV-F.

The sweep covers $M_t \in \{8, 10, 12, 14, 16\}$ for the TXA and $N_r \in \{1, 2, \ldots, 8\}$ for the RXA, yielding 40 combinations. Only the DC-to-DC optimization is applied. The DC power budget is set to $P_t^{\mathrm{DC}} = 1200$ W, which exceeds the maximum DC consumption of the largest array configuration ($16 \times 16 = 256$ PAs, each consuming up to $h(1.0) = 4.36$ W, totaling 1116 W), ensuring that the power budget does not artificially constrain any configuration. For the smallest 8×8 TXA considered in this sweep, the diagonal aperture dimension is $D = 8 \cdot (0.6\lambda) \cdot (2)^{1/2} = 0.361$ m. The corresponding reactive near-field boundary is $0.62(D^3/\lambda)^{1/2} = 0.583$ m. Therefore, $d = 0.5$ m lies within the near-field region even for the smallest TXA, and hence for all larger TXA configurations considered in Fig. 9.

To quantify the receiver-side utilization, we introduce the rectifier utilization efficiency (RUE), defined as [31]

$$\mathrm{RUE} = \frac{\sum_{n=1}^{N} P_{\mathrm{RX},n}^{\mathrm{DC},port}}{N \cdot P_{\mathrm{rect,peak}}} \tag{27}$$

where $P_{\mathrm{rect,peak}}$ is the peak DC output of a single rectifier. While the DC-to-DC efficiency $\eta_{\mathrm{DC-DC}}$ measures the system-level end-to-end performance (ratio of total received DC to total consumed DC), RUE captures how effectively each individual rectifier is utilized relative to its maximum capacity. These two metrics are complementary: a high $\eta_{\mathrm{DC-DC}}$ does not guarantee high RUE, and vice versa.

Fig. 9 presents the contour maps of four metrics as functions of M_t and N_r. The DC-to-DC efficiency [see Fig. 9(a)] increases with larger N_r and smaller M_t. This is because a larger TXA, while delivering more power to the RXA, consumes disproportionately more DC power at the PA stage, resulting in a net decrease in end-to-end efficiency. Conversely, the total received DC power [see Fig. 9(c)] increases with both M_t and N_r due to the larger combined aperture, revealing a clear tradeoff between efficiency and received power.

The RUE [see Fig. 9(b)] exhibits a distinct behavior: it remains close to 100% when N_r is small, but drops sharply when N_r is large and M_t is small. This occurs because a small TXA produces a broad beam with limited focusing capability. When such a beam focuses a large RXA, the received power is distributed thinly across many rectifier elements, causing each rectifier to operate far below its peak PCE. In contrast, a large TXA focuses the beam more effectively in the near field, delivering sufficient power to each rectifier even when the RXA is large, thereby maintaining high RUE. The TX DC power [see Fig. 9(d)] confirms the expected trend: larger arrays on both sides consume more DC power.

To navigate the tradeoff between DC-to-DC efficiency and received DC power, we employ a Pareto front analysis, as shown in Fig. 10. A design point is Pareto-optimal if no other configuration simultaneously achieves both higher effi-

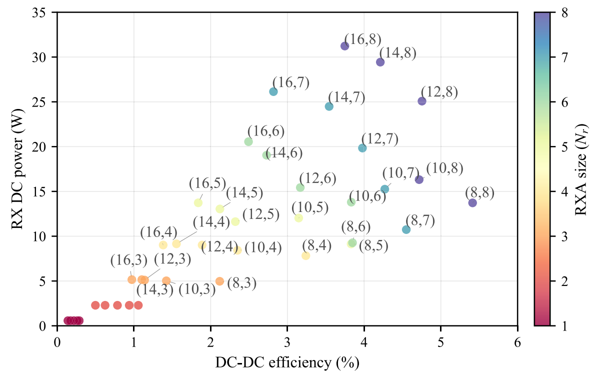

Fig. 10. DC-to-DC efficiency versus received DC power for all TXA–RXA combinations at d = 0.5 m. Each marker is colored by N_r.

ciency and higher received power; improving one objective necessarily degrades the other. The Pareto-optimal configurations are $(M_t, N_r) = (8, 8)$, $(12, 8)$, $(14, 8)$, and $(16, 8)$, all sharing $N_r = 8$, indicating that maximizing the RXA size is always beneficial. The tradeoff is governed solely by the TXA size. Considering the balance between efficiency and received power across the Pareto front, we select $(M_t, N_r) = (12, 8)$ as the operating configuration for the subsequent scenarios.[7]

C. Efficiency Comparison Under Various Scenarios

This section compares the three optimizations as Fig. 11—RF-to-RF, RF-to-DC, and DC-to-DC—under varying propagation conditions using the array configuration $(M_t, N_r) = (12, 8)$ selected in the previous subsection. For the 12 × 12 TXA with M = 144 PAs, the minimum DC consumption is $M \cdot h(0) = 144 \times 1.46 = 210$ W, and the maximum at full power is $M \cdot h(1.0) = 144 \times 4.36 = 628$ W. The DC power budget is set to $P_t^{\mathrm{DC}} = 400$ W, which is a reasonable intermediate value that ensures magnitude tapering across the array elements. For a fair comparison, the RF power budget P_t^{RF} of the PTE and TCE optimizations is set to the RF transmit power consumed by the DC-to-DC solution at each condition. Two propagation parameters are swept independently: the distance d from 0.5 to 3.0 m at broadside ($\theta = 0°$), and the azimuth angle θ from 0° to 60° at d = 0.5 m, as illustrated in Fig. 12.

Fig. 11(a) shows the three efficiency metrics as a function of distance. All metrics decrease monotonically with increasing distance due to the growing path loss. PTE shows the highest value trivially since it only accounts for the RF power transfer from the TXA to the RXA, without considering any nonlinearities. TCE is consistently lower than PTE because it additionally accounts for the rectifier PCE and the RX antenna radiation efficiency $\eta_{\mathrm{RX}}^{\mathrm{rad}}$ in the rad-to-port path. The DC-to-DC efficiency, which further includes the PA DC consumption in the denominator, reaches 4.53% at its peak (d = 0.5 m and $\theta = 0°$). Fig. 11(b) presents the SDP relaxation upper bound $\bar{P}_{\mathrm{DC}}$ and the recovered solution P_{DC}^{*} for the RF-to-DC and DC-to-DC frameworks. At short distances where the channel exhibits high rank (rank = 4 for DC-to-DC at d = 0.5 m), the SDR produces a higher rank S^*, resulting in a gap between $\bar{P}_{\mathrm{DC}}$ and P_{DC}^{*}. Nevertheless, the recovery ratio $\rho_{\mathrm{rec}} = P_{\mathrm{DC}}^{*}/\bar{P}_{\mathrm{DC}}$ remains above 97.5%, confirming the effectiveness of the SCA-based rank-one recovery. The RF-to-DC framework, which is free of the PA power constraint, which leads to low rank conditions, achieves near-perfect recovery ($\rho_{\mathrm{rec}} \geq 99.1\%$). As the distance increases beyond 1.5 m, the channel becomes increasingly rank-deficient; the SDP solution naturally converges to rank one, and all three methods yield nearly identical received DC power.

Fig. 11(c) and (d) presents the corresponding results for the azimuth angle sweep at d = 0.5 m. All metrics degrade with increasing θ due to the element gain roll-off. The bound–recovery gap narrows accordingly, with ρ_{rec} remaining above 97.1% across all angles.

Overall, both the distance and azimuth angle sweeps exhibit smooth and monotonic decreases in all efficiency metrics, consistent with the expected behavior. The SCA rank-one recovery achieves $\rho_{\mathrm{rec}} \geq 97.1\%$ across all tested conditions for the DC-to-DC framework, confirming that the SDR relaxation gap is negligible in practice.

The preceding analysis evaluates each framework by its own efficiency metric; however, to assess which optimization produces the best excitation vector in terms of actual end-to-end performance, all three must be compared under the same $\eta_{\mathrm{DC-DC}}$ criterion. Since the RF-to-RF and RF-to-DC frameworks do not impose PA constraints, their optimal excitation vectors may contain per-element RF powers exceeding the PA model max RF power (30 dBm). To ensure a fair comparison, PA clipping is applied—the magnitude of each element is limited to 1 W while the phase is preserved—and the clipped excitation is refed through the channel and an extended rectifier model to recompute the DC-to-DC efficiency.[8] Fig. 13 shows the resulting comparison. At d = 0.5 m, the DC-to-DC optimization achieves $\eta_{\mathrm{DC-DC}} = 4.53\%$, compared with 3.45% for RF-to-DC and 3.06% for RF-to-RF—representing relative improvements of 31.3% and 48.0%, respectively—confirming that jointly accounting for the PA and rectifier nonlinearities does yield a more efficient excitation. As the distance or angle increases, the received power decreases, and the nonlinear effects diminish, causing the three methods to converge beyond $d \geq 1.5$ m or $\theta \geq 40°$.

Notably, Fig. 11(b) shows that the received DC power of the DC-to-DC and RF-to-DC frameworks is nearly identical at short distances (18.1 versus 18.9 W at d = 0.5 m). One might expect a tradeoff where the RF-to-DC framework, unconstrained by the PA, delivers substantially more received power at the cost of TX-side efficiency. In practice, however, the received power advantage of RF-to-DC is marginal, while the DC-to-DC framework achieves a 31.3% higher end-to-end efficiency by producing a PA-aware excitation that significantly reduces the TX DC consumption. This indicates

[7]For this configuration, the average computation times per instance are approximately 2 s (RF-to-RF), 2 min 15 s (RF-to-DC), and 4 min 37 s (DC-to-DC), measured in MATLAB with convex solvers.

[8]This post hoc clipping is not a rigorous reoptimization; a stricter approach would embed the PA and rectifier models into each framework. Since those frameworks are formulated without such models, the clipping-based re-evaluation provides the most reasonable basis for a unified comparison.

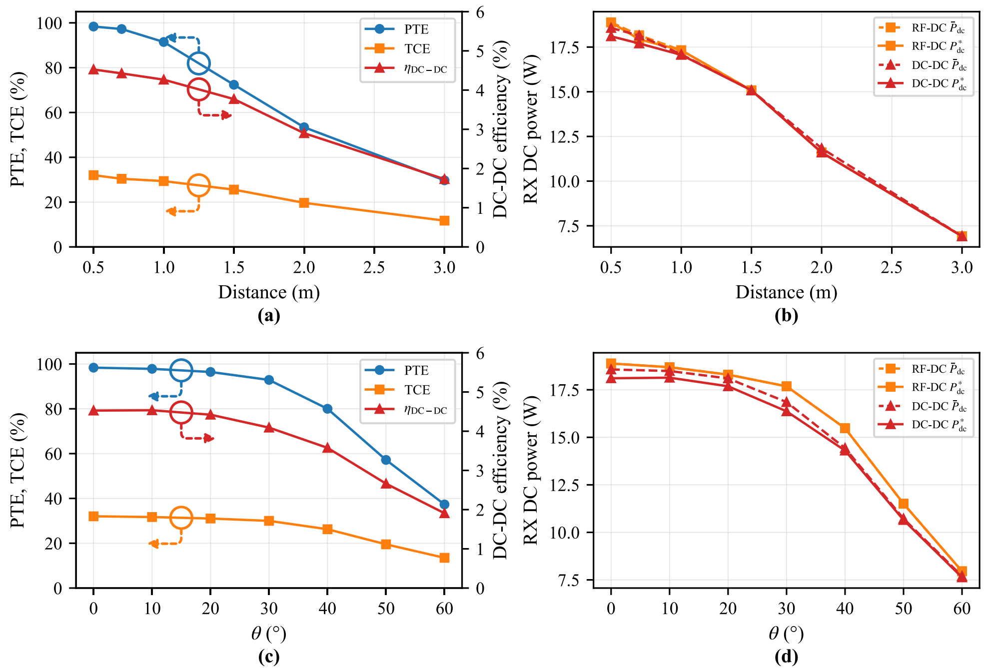

Fig. 11. Comparison of three optimization frameworks under varying propagation conditions with $(M_t, N_r) = (12, 8)$ and $P_t^{\mathrm{DC}} = 400$ W. (a) PTE, TCE, and $\eta_{\mathrm{DC-DC}}$ versus distance. (b) SDP upper bound $\bar{P}_{\mathrm{DC}}$ and recovered P^*_{DC} versus distance. (c) Efficiency metrics versus azimuth angle at $d = 0.5$ m. (d) SDP bound and recovered versus azimuth angle.

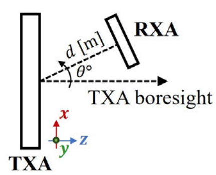

Fig. 12. Simulation geometry. The RXA is displaced by distance d along the boresight direction and rotated by azimuth angle θ.

that the DC-to-DC optimization is not merely a different efficiency–power tradeoff point, but demonstrates a consistent system-level advantage in the near-field regime.

D. Stage-Level Efficiency Breakdown

To show how the end-to-end gain is distributed across the conversion chain, Table III decomposes $\eta_{\mathrm{DC-DC}}$ into its three stage efficiencies following (10) at the representative operating point $(M_t, N_r) = (12, 8)$, $d = 0.5$ m, $\theta = 0°$, and $P_t^{\mathrm{DC}} = 400$ W. Each framework exhibits a clear efficiency peak precisely at the stage of its objective targets—RF-to-RF at the air-interface, RF-to-DC at the rectifier, and DC-to-DC at the PA. For the RF-to-RF and RF-to-DC frameworks, the stages absent from their objectives (marked by †) are evaluated by post hoc substitution into the $h(\cdot)$ and $f(\cdot)$.

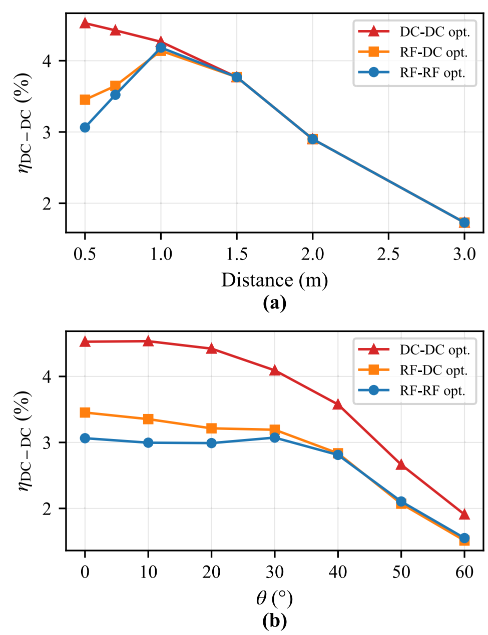

Fig. 13. Fair comparison of the three optimization frameworks evaluated under the same $\eta_{\mathrm{DC-DC}}$ metric. PA clipping is applied to the RF–RF and RF–DC excitation vectors prior to re-evaluation versus (a) distance and (b) azimuth angle.

E. Efficiency Comparison Under Varying Power Budgets

This section investigates the effect of the DC power budget P_t^{DC} on the DC-to-DC optimization. From a system design perspective, when the size and geometry of the TXA and RXA are fixed, the DC power budget is a critical design parameter that governs the operating point of the system. In the configuration of $(M_t, N_r) = (12, 8)$, $d = 0.5$ m, and $\theta = 0°$, the budget is swept over $P_t^{\mathrm{DC}} \in \{300, 400, 500, 600\}$ W; budgets below 300 W are infeasible as they cannot satisfy the minimum PA quiescent consumption of 210 W.

TABLE III
STAGE-LEVEL EFFICIENCY BREAKDOWN $(M_t, N_r) = (12, 8)$, $d = 0.5$ M, $\theta = 0°$, AND $P_t^{\mathrm{DC}} = 400$ W

Framework	PA $\eta_{\mathrm{DC\text{-}RF}}$	Air $\eta_{\mathrm{RF\text{-}RF}}$	Rect. $\eta_{\mathrm{RF\text{-}DC}}$	End-to-end $\eta_{\mathrm{DC\text{-}DC}}$
RF-to-RF	12.9%†	96.0%	30.5%†	3.06%
RF-to-DC	11.7%†	89.2%	40.8%	3.45%
DC-to-DC	16.4%	92.2%	37.0%	4.53%

† Post-hoc value from substituting into $h(\cdot)$ or $f(\cdot)$ (not optimized).

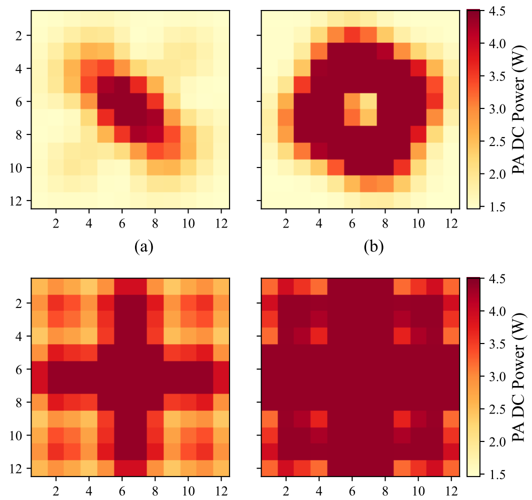

Fig. 14. Per-element PA DC power distribution of the 12×12 TXA optimized by the DC–DC framework at $d = 0.5$ m and $\theta = 0°$ for P_t^{DC} = (a) 300, (b) 400, (c) 500, and (d) 600 W.

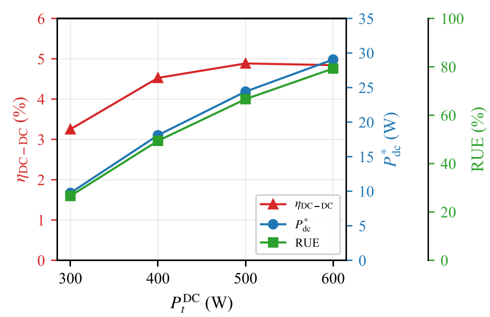

Fig. 15. DC–DC efficiency and received DC power P_{DC}^* versus DC power budget P_t^{DC} with $(M_t, N_r) = (12, 8)$ at $d = 0.5$ m and $\theta = 0°$.

Fig. 14 shows the per-element PA DC power distribution optimized by the DC-to-DC framework across the 12×12 TXA for each budget. As expected for the broadside configuration, the distributions exhibit symmetry.

Fig. 15 summarizes the corresponding $\eta_{\mathrm{DC-DC}}$ and P_{DC}^* as functions of P_t^{DC}. The received DC power increases monotonically from 9.8 W at 300 W to 29.1 W at 600 W. The efficiency peaks at $P_t^{\mathrm{DC}} = 500$ W ($\eta_{\mathrm{DC-DC}} = 4.88\%$) and slightly decreases at 600 W (4.84%). At 600 W, the mean per-PA DC consumption reaches 4.17 W out of the 4.36 W maximum, indicating that the TXA is operating near the PA saturation limit, while RUE remains at 79.3%, so the RXA still has headroom. The weak peak shape in this configuration

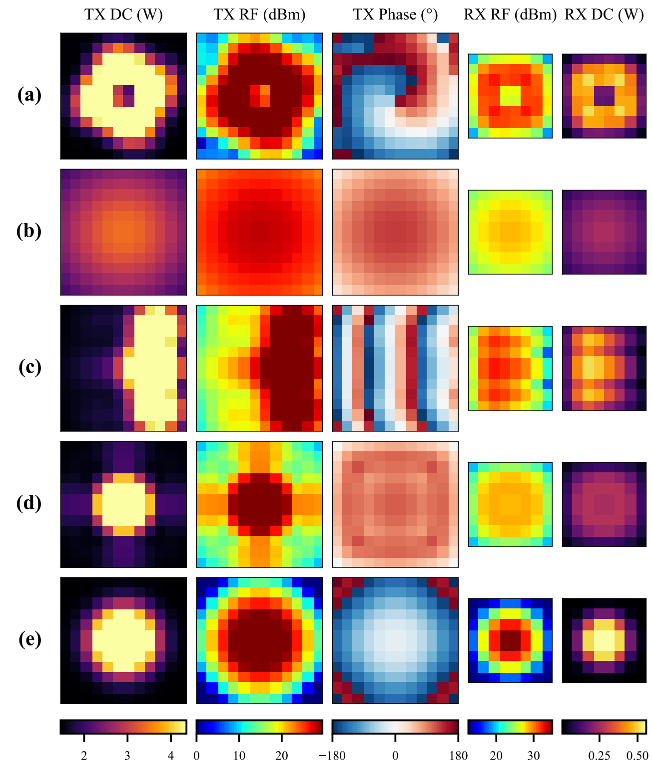

Fig. 16. Per-element excitation and received power maps for five cases. Columns from left to right: TX DC power (W), TX RF power (dBm), TX phase (°), RX RF power (dBm), and RX DC power (W). Each array is viewed from its own front face. (a) DC–DC, $d = 0.5$ m, and $\theta = 0°$. (b) DC–DC, $d = 2.0$ m, and $\theta = 0°$. (c) DC–DC, $d = 0.5$ m, and $\theta = 30°$. (d) RF–DC (clipped), $d = 0.5$ m, and $\theta = 0°$. (e) RF–RF (clipped), $d = 0.5$ m, and $\theta = 0°$.

is therefore dictated by the TX-side PA saturation rather than the RX-side rectifier saturation. Since this RX-side headroom is finite, it can be breached by enlarging the TXA to deliver more RF power, which pushes RUE toward 100%, as shown in Fig. 9(b) for increasing M_t at fixed N_r. However, this comes at the cost of a reduced $\eta_{\mathrm{DC-DC}}$ [see Fig. 9(a)]—an inherent tradeoff between RX utilization and end-to-end efficiency.

F. Excitation Pattern Analysis

Fig. 16 visualizes the per-element excitation patterns for five representative cases. Each row shows, from left to right, the TX PA DC power, TX radiated RF power, TX phase, RX radiated RF power, and RX DC power. Each array is depicted as viewed from its own front face. Rows (a)–(c) correspond to the DC-to-DC optimization under different propagation conditions, while rows (d) and (e) show the clipped RF-to-DC and RF-to-RF excitations at the same condition as (a) for direct comparison.

Fig. 16(a) and (b) illustrates the transition from near-field to far-field behavior. At $d = 0.5$ m (a), the optimizer produces a nontrivial magnitude distribution with a complex phase pattern, and the RX DC power is broadly distributed across the 8×8 RXA, confirming effective near-field focusing. At $d = 2.0$ m (b), the channel approaches rank one, and the excitation converges toward a conventional far-field pattern with a narrow phase range and reduced received power. This transition from near-field focusing to far-field beamforming is consistent with the expected qualitative behavior. Row (c) shows the $\theta = 30°$ case, where a phase gradient is clearly visible across the TXA columns, steering the beam off broadside. The resulting RX pattern exhibits a corresponding asymmetry.

Comparing Fig. 16(a), (d), and (e) at the same condition ($d = 0.5$ m and $\theta = 0°$) reveals the fundamental differences among the three frameworks. The RF-to-DC excitation (d) concentrates power toward the center with a relatively smooth phase distribution, as the optimizer focuses on maximizing the rectifier output without PA awareness. The RF-to-RF excitation (e) shows a similarly centered magnitude pattern but with a nearly uniform phase, since PTE maximization does not benefit from phase diversity. In contrast, the DC-to-DC excitation (a) distributes power more broadly across the TXA, placing each PA at a favorable operating point while maintaining a complex phase pattern that effectively utilizes the full RXA aperture.

G. Design Guidelines

The array-size analysis in Section IV-B guides the choice of the TXA and RXA sizes. Enlarging the RXA raises both the received DC power and the end-to-end efficiency, but it lowers the RUE when the TXA cannot focus enough power onto the larger aperture, leaving each rectifier underutilized. Enlarging the TXA restores focusing and increases the received power, yet it lowers the efficiency, since a larger array consumes more DC power at the PA stage.[9] In short, the RXA should be enlarged as far as the application allows, as long as the RUE stays acceptable. The TXA is then sized to keep the RUE high while meeting the target received power.

The propagation analysis in Section IV-C highlights the role of the operating regime. As the distance grows, the channel transitions from near-field focusing to far-field beamforming, and the three frameworks converge. The near-field excitation requires magnitude tapering and phase shaping, whereas the far-field excitation reduces to conventional beamforming. Unlike conventional approaches, the proposed framework provides a design solution across both regimes.

The power-budget analysis in Section IV-E shows that, for a fixed geometry, the DC power budget P_t^{DC} determines the operating point on the efficiency–power curve. Since the optimum budget varies with the scenario, and the DC-to-DC efficiency, P_{DC}^{*}, and the RUE all change considerably with P_t^{DC}, the budget should be determined by sweeping it and jointly considering these three metrics, yielding a system-optimized design.

V. Experimental Validation

A. Measurement Setup

This section validates that the rank-one excitation vector obtained from the proposed DC-to-DC framework delivers the expected performance on real hardware. The overall measurement setup is shown in Fig. 17: a 16 × 16 planar TXA

[9]The added DC consumption of a larger TXA can be mitigated by switching idle PAs to an OFF or reduced-bias state [26], [44].

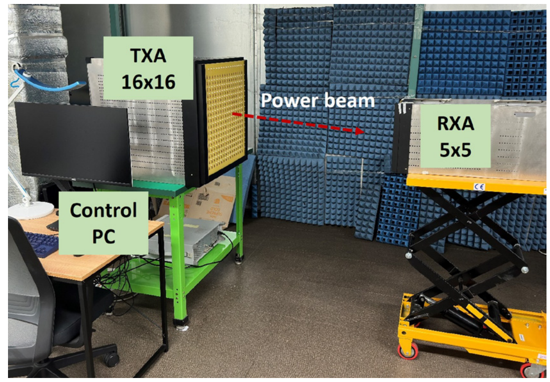

Fig. 17. Overall configuration in the laboratory free-space environment, with the 16 × 16 TXA, 5 × 5 RXA, and control PC.

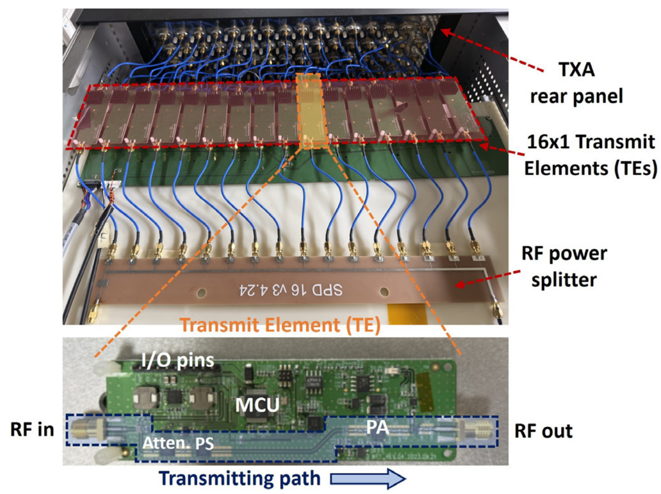

Fig. 18. Transmitter side. Close-up of a single TE showing the cascade of attenuator (Atten), PS, and PA on the PCB, integrated into the 16 × 16 TXA.

operating at 5.64 GHz, a 5 × 5 RXA whose elements use the half-wave rectifier characterized in Section IV-A, and a control PC that drives the TXA excitation and collects the RX DC readings. The system follows the architecture described in [40]. Since the Pareto-optimal $(M_t, N_r) = (12, 8)$ selected in Section IV is not realizable on the fabricated array, the measurements employ the (16, 5) configuration, which matches the fabricated prototype. The measurements are performed in a laboratory free-space environment.

Fig. 18 details the transmitter side. The close-up view shows a single TE, where an attenuator (Atten), a PS, and a PA are cascaded on the PCB. 16 × 1 TEs form a 1-D subarray, which are then stacked to create the full 16 × 16 TXA. Per-element control signals from the PC set the attenuation and phase of each TE so that the optimized excitation vector x_t^{*} is realized at the antenna ports.

Fig. 19 illustrates the receiver-side measurement scheme. The formulation assumes ideal DC combining at the RXA, but the prototype does not implement an actual DC summing network. As shown in Fig. 19(a), while the TXA continuously transmits the optimized beam, a single rectifier is manually moved from one RXA port to the next, and the remaining 24 ports are terminated by 50-Ω loads to preserve the array

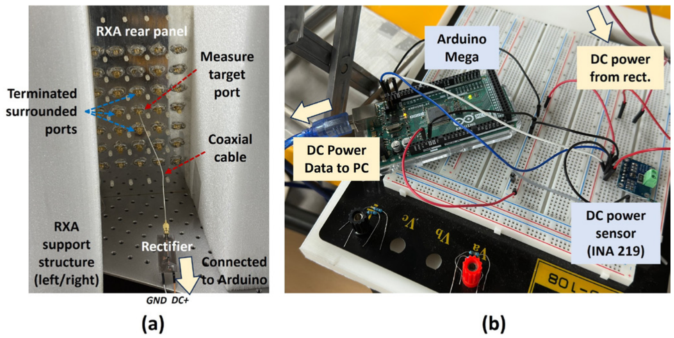

Fig. 19. Receiver-side measurement. (a) Single rectifier is sequentially placed at each of the 25 RXA ports while the remaining ports are 50-Ω-terminated, emulating ideal DC combining. (b) Rectifier DC output is monitored by an INA219 current–voltage sensor via an Arduino Mega that streams the readings to the PC.

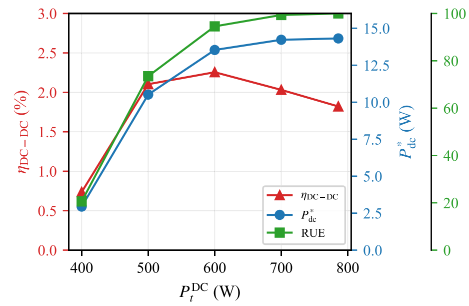

Fig. 20. DC–DC efficiency, received DC power, and RUE versus DC power budget for $(M_t, N_r) = (16, 5)$ at $d = 0.5$ m and $\theta = 0°$.

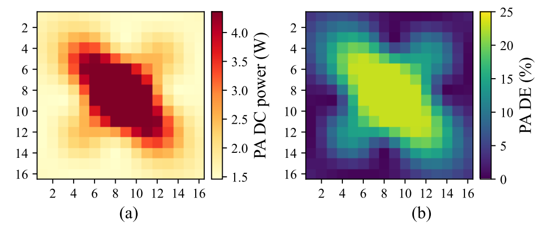

Fig. 21. Per-element maps of the 16×16 TXA optimized by the DC-to-DC framework at $P_t^{DC} = 600$ W, $d = 0.5$ m, and $\theta = 0°$. (a) PA DC power. (b) PA DE (mean = 13.0%).

loading conditions. The rectifier DC output [see Fig. 19(b)] is read by an INA219 current-voltage sensor through an Arduino Mega that streams the per-port reading to the PC. The 25 individual port readings are then summed in postprocessing to obtain the total received DC power, equivalent to the ideal DC combining assumed in the formulation.

B. Measurement Procedure

For each measurement point, the rank-one excitation vector x_t^* obtained from the DC-to-DC optimization in Section III-D is applied directly to the TXA through the per-element control interface. Two sweeps are performed: the distance sweep varies $d \in \{0.5, 0.7, 1.0, 1.5\}$ m at broadside ($\theta = 0°$), and the azimuth sweep varies $\theta \in \{0°, 20°, 40°, 60°\}$ at $d = 0.5$ m.

Since the assembled TXA does not permit direct per-element DC probing, the TX DC consumption is obtained by passing each element's measured RF port power through the PA model $h(\cdot)$ in (26), whereas the RX DC power is measured directly via the per-port sweep of Fig. 19. The measurement-based models $h(\cdot)$ and $f(\cdot)$ characterized in Section IV-A are thus carried through both the simulation and the experiment without recharacterization, with $f(\cdot)$ physically embodied by the fabricated rectifiers.

C. Analysis of the (16, 5) Regime

The fabricated $(16, 5)$ configuration differs from the previous $(12, 8)$, so the result is expected to differ. The TXA is enlarged from 144 to 256 PAs, while the RXA is reduced from 64 to 25 rectifiers. This TX/RX size imbalance shifts the system into a different operating regime, which is analyzed next to determine the appropriate DC power budget.

Following the same procedure as Section IV-E, the DC power budget P_t^{DC} is swept from 400 to 800 W in 100-W increments, with the propagation parameters fixed at $d = 0.5$ m and $\theta = 0°$.[10] Fig. 20 shows the resulting η_{DC-DC}, P_{DC}^*, and RUE. The received DC power rises from 2.9 W at 400 W to 13.5 W at 600 W, then saturates at 14.3 W near $P_t^{DC} \approx 700$ W, at which point RUE reaches 99.4%. Beyond this point, further increases in P_t^{DC} produce negligible gain in P_{DC}^*, and the optimizer does not fully consume the budget: the actual TX DC consumption at an 800 W budget is 785.8 W. Consequently, η_{DC-DC} exhibits a pronounced peak at $P_t^{DC} = 600$ W, reaching 2.26%, beyond which additional DC input is wasted as PA quiescent overhead. Unlike the $(12, 8)$ case in Fig. 15, where the peak is only faintly visible because the PA saturation cap is reached before the RXA saturates, here the 25 rectifiers collectively saturate while the 256 PAs still operate below their limit, producing a clearer peak.

This peak, $\eta_{DC-DC} = 2.26\%$, is the maximum end-to-end efficiency achievable on the fabricated $(16, 5)$ hardware.[11] Its structure is revealed in Fig. 21, which shows the per-element PA DC power [see Fig. 21(a)] and PA DE [see Fig. 21(b)] distributions at $P_t^{DC} = 600$ W. The central elements are driven up to 4.36 W (near PA saturation) to form the near-field focus and reach DE above 20%, while the edge elements remain near the quiescent value of 1.46 W with DE below 5%, as total mean DE is 13.0%. Given the above, the measurements in the following subsection are performed at $P_t^{DC} = 600$ W.

D. Measurement Results

Fig. 22 compares the simulated and measured η_{DC-DC} for the DC-to-DC optimized excitation across both sweeps.

In the distance sweep [see Fig. 22(a)], both the simulation and the measurement exhibit a monotonic decrease with distance, with the measurement ranging from 2.15% at $d = 0.5$ m to 1.85% at $d = 1.5$ m. The measured values remain 5%–7%

[10] The reference scenario ($d = 0.5$ m and $\theta = 0°$) is retained across the configuration change for consistency throughout this article, since it supports a secure near-field condition for general scenarios.

[11] This value is limited by the prototype's commercial PA and simple rectifier, not by the framework itself; Section VI-B projects a peak DC-to-DC efficiency of 32.95% under SOTA device models.

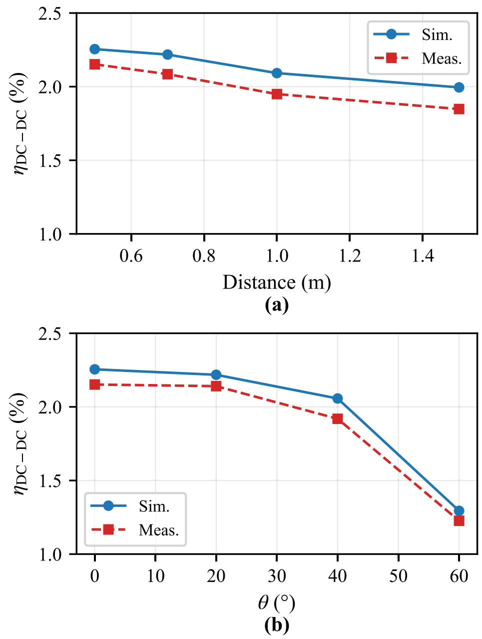

Fig. 22. DC–DC efficiency obtained from simulation and measurement for the 16 × 16 TXA and 5 × 5 RXA at P_t^{DC} = 600 W. (a) Distance sweep at $\theta = 0°$. (b) Azimuth angle sweep at $d = 0.5$ m.

below the simulated ones across the entire range, which is within the various measurement nonidealities in the laboratory environment.

In the azimuth sweep [see Fig. 22(b)], $\eta_{\text{DC-DC}}$ drops more steeply with steering angle, from 2.15% at broadside to 1.23% at $\theta = 60°$. The measurement tracks the simulation with a comparable 3%–7% gap. Overall, the measured results confirm that the excitation produced by the proposed DC-to-DC framework delivers the expected end-to-end performance on the fabricated hardware, with the measured peak of 2.15% at the reference operating point within 5% of the framework-predicted 2.26%.

VI. Discussion

A. Modeling Scope and Deployment

On the transmit side, only the PA consumption is modeled, for two reasons: it dominates the front-end power budget, and it is the only DC consumption that varies with the excitation. The attenuators, PSs, and digital control circuitry (e.g., SPI and MCU) draw small, *fixed power* independent of the excitation, so characterizing them would not affect the optimization; they are therefore omitted. On the receive side, the formulation assumes ideal lossless DC combining, which does not capture the output-voltage mismatch and DC–DC converter losses present in practical rectenna arrays.

The framework is derived for a free-space LoS channel, but the propagation environment enters only through the channel matrix $\mathbf{G}$. In the presence of clutter or backscatter, the same formulation applies once $\mathbf{G}$ is replaced by the corresponding multipath or measured channel, with no change to the optimization itself.

TABLE IV

Simulated DC-to-DC Performance of the $(M_t, N_r) = (12, 8)$ System at $d = 0.5$ m and $\theta = 0°$: Prototype Versus SOTA

	Prototype (Sec. IV)	SOTA (projected)
PA	Commercial class-AB	GaN Doherty [45]
Peak DE	32.2%	69.8%
Rectifier	Half-wave Schottky	Wideband GaN [46]
Peak PCE	45.4%	71.0%
P_t^{DC}	500 W	140 W
Simulated $\eta_{\text{DC-DC}}$	4.88%	32.95%

B. Projected Performance With State-of-the-Art Devices

The primary contributions of this work are the optimization framework and the accompanying design analysis; the absolute end-to-end efficiency is not itself a design target. For this reason, the experimental validation employs a commercial PA and a simple half-wave rectifier, which suffice to verify the framework but are not high-efficiency parts. Since the framework depends only on the measurement-based device models $h(\cdot)$ and $f(\cdot)$, it is possible to project the efficiency attainable when SOTA devices are substituted. This section reports such a projection for a representative 5.8-GHz-band SOTA PA and rectifier. The device models are extracted by carefully digitizing the measured curves reported in the cited References, so the results are simulation-based projections rather than measured performance.

Following the same modeling procedure as Section IV-A, only the device data are replaced. The PA model adopts a high-efficiency GaN Doherty PA [45]; the affine $h(p) = \alpha p + \beta$ is a least-squares fit over its high-efficiency power back-off range, with the slight plateau curvature absorbed as regression residual, thereby preserving the affine PA constraint of the formulation. The rectifier model adopts a wideband, high-PCE GaN rectifier [46], fit by the same concave PWL procedure. All other settings, such as the channel model and array size, remain identical.

Under the same scenario as Section IV ($(M_t, N_r) = (12, 8)$, $d = 0.5$ m, $\theta = 0°$), applying the proposed framework with the SOTA PA and rectifier yields a projected peak DC-to-DC efficiency of 32.95% at a DC power budget of $P_t^{\text{DC}} = 140$ W. Table IV summarizes this projection against the corresponding Section IV result obtained with the prototype device models.

VII. Conclusion and Future Works

This article presented an end-to-end DC-to-DC efficiency optimization framework for CW-based MIMO WPT systems that jointly accounts for PA and rectifier nonlinearities. Using an affine PA model and a concave PWL rectifier model extracted from measurements, the optimization was cast as an SDP under a DC power budget constraint, and an SCA procedure was developed to recover a feasible rank-one excitation vector from the relaxed solution. The SDP objective serves both as an upper bound on the achievable DC power and as a warm start for the SCA iterations, yielding a recovery ratio exceeding 97% across all tested conditions.

The RF-to-RF, RF-to-DC, and DC-to-DC formulations were systematically compared across various array-size, propagation, and power-budget scenarios. Jointly accounting for the PA and rectifier in the objective produces excitations that deliver 31% and 48% higher end-to-end efficiency than the RF-to-DC and RF-to-RF counterparts, respectively, at $d = 0.5$ m in the near-field regime. Experimental validation on a fabricated 16 × 16 TXA and 5 × 5 rectenna confirmed that the measured DC-to-DC efficiency tracks the simulation across both distance and azimuth sweeps, verifying the practical applicability of the proposed framework for MIMO WPT system design.

To summarize, DC-to-DC efficiency is among the most important end-to-end metrics for WPT systems, but it has been addressed only indirectly in prior works. This framework takes it as the primary design objective, and the resulting upper bound on the achievable DC power can serve as a benchmark for future MIMO WPT designs.

Future work will include modeling realistic DC combining, with the development of low-loss DC-combining circuits at the device level, and pursuing real-time algorithms that approach the upper bound presented in this work.

Appendix

A. Proof of Affine Minorizer Properties

This appendix derives the affine minorizer $\hat{q}_n(x_t; x_t^{(i)})$ used in the SCA subproblem (21). Define $\varphi_n(x_t) = |g_n^H x_t|^2/Z$, which represents the received RF power at the nth rectifier. This function is convex in x_t, since it is a nonnegative scaling of the squared modulus of a linear function.

By the first-order condition for convex functions

$$\varphi_n(x_t) \geq \varphi_n\left(x_t^{(i)}\right) + \mathrm{Re}\left(\nabla_{x_t}\varphi_n\left(x_t^{(i)}\right)^H\left(x_t - x_t^{(i)}\right)\right) \tag{28}$$

for all x_t, where $\nabla_{x_t} \triangleq 2\,\partial/\partial x_t^*$ denotes the Wirtinger conjugate gradient, with x_t and x_t^* treated as independent variables. Applying this operator to φ_n gives

$$\nabla_{x_t}\varphi_n(x_t) = \frac{2}{Z} g_n\left(g_n^H x_t\right). \tag{29}$$

Substituting (29) into (28) and simplifying

$$\begin{aligned}\varphi_n(x_t) &\geq \frac{\left|g_n^H x_t^{(i)}\right|^2}{Z} + \frac{2}{Z}\mathrm{Re}\left(\left(g_n^H x_t^{(i)}\right)^* g_n^H\left(x_t - x_t^{(i)}\right)\right)\\ &= \frac{2}{Z}\mathrm{Re}\left(\left(g_n^H x_t^{(i)}\right)^* g_n^H x_t\right) - \frac{\left|g_n^H x_t^{(i)}\right|^2}{Z}\\ &= \hat{q}_n\left(x_t; x_t^{(i)}\right).\end{aligned} \tag{30}$$

This confirms the global lower bound property: $\hat{q}_n(x_t; x_t^{(i)}) \leq p_{\mathrm{RX},n}(x_t)$ for all x_t. The tangent point agreement follows directly by setting $x_t = x_t^{(i)}$:

$$\begin{aligned}\hat{q}_n\left(x_t^{(i)}; x_t^{(i)}\right) &= \frac{2\left|g_n^H x_t^{(i)}\right|^2}{Z} - \frac{\left|g_n^H x_t^{(i)}\right|^2}{Z}\\ &= \frac{\left|g_n^H x_t^{(i)}\right|^2}{Z} = p_{\mathrm{RX},n}\left(x_t^{(i)}\right).\end{aligned} \tag{31}$$

TABLE V
Concave PWL Parameters of the Rectifier Model $f(\cdot)$

k	P_{rf} range (dBm)	P_{rf} range (mW)	a_k	b_k (mW)
1	[0, 23]	[1.0, 199.5]	0.460	−1.20
2	[23, 28]	[199.5, 631.0]	0.373	16.31
3	[28, 30.5]	[631.0, 1122.0]	0.327	45.19
4	[30.5, 31]	[1122.0, 1258.9]	0.291	86.01
5	[31, 31.5]	[1258.9, 1412.5]	0.210	187.26
6	[31.5, 32]	[1412.5, 1584.9]	0.161	256.73
7	[32, 32.5]	[1584.9, 1778.3]	0.096	359.57
8	[32.5, 33]	[1778.3, 1995.3]	0.086	378.13
9	[33, 33.5]	[1995.3, 2238.7]	0.061	428.16
10	[33.5, 34]	[2238.7, 2511.9]	0.033	490.09
11	[34, 34.5]	[2511.9, 2818.4]	−0.043	680.00
12	[34.5, 35]	[2818.4, 3162.3]	−0.075	771.79

Finally, $\hat{q}_n(x_t; x_t^{(i)})$ is affine in x_t because it consists of $\mathrm{Re}(\cdot)$ applied to a linear function of x_t plus a constant.

B. Convergence of the SCA Iterates

This appendix proves that Algorithm 1 produces a monotonically nondecreasing objective sequence that converges to a KKT stationary point of (19).

Let

$$F(x_t) = \sum_{n=1}^{N} f\left(p_{\mathrm{RX},n}(x_t)\right) \tag{32}$$

be the original objective and

$$\tilde{F}\left(x_t; x_t^{(i)}\right) = \sum_{n=1}^{N} f\left(\hat{q}_n\left(x_t; x_t^{(i)}\right)\right) \tag{33}$$

be the surrogate objective at iteration i. Define $x_t^{(i+1)} = \arg\max \tilde{F}(x_t; x_t^{(i)})$ subject to the constraints in (21).

Step 1 (Lower Bound): Since $\hat{q}_n(x_t; x_t^{(i)}) \leq p_{\mathrm{RX},n}(x_t)$ for all x_t (see Appendix A) and $f(\cdot)$ is nondecreasing over the valid operating range

$$F\left(x_t^{(i+1)}\right) \geq \tilde{F}\left(x_t^{(i+1)}; x_t^{(i)}\right). \tag{34}$$

Step 2 (Optimality of Update): Since $x_t^{(i+1)}$ maximizes the surrogate and $x_t^{(i)}$ is feasible

$$\tilde{F}\left(x_t^{(i+1)}; x_t^{(i)}\right) \geq \tilde{F}\left(x_t^{(i)}; x_t^{(i)}\right). \tag{35}$$

Step 3 (Tangent Point Agreement): By the tangent point property, $\hat{q}_n(x_t^{(i)}; x_t^{(i)}) = p_{\mathrm{RX},n}(x_t^{(i)})$, so

$$\tilde{F}\left(x_t^{(i)}; x_t^{(i)}\right) = F\left(x_t^{(i)}\right). \tag{36}$$

Combining (34)–(36)

$$F\left(x_t^{(i+1)}\right) \geq \tilde{F}\left(x_t^{(i+1)}; x_t^{(i)}\right) \geq \tilde{F}\left(x_t^{(i)}; x_t^{(i)}\right) = F\left(x_t^{(i)}\right). \tag{37}$$

Thus $\{F(x_t^{(i)})\}$ is monotonically nondecreasing. Since $F(x_t) \leq \bar{P}_{\mathrm{DC}}$ for all feasible x_t (the SDP upper bound), the sequence is bounded above and therefore converges. By standard SCA convergence theory [47], every limit point of $\{x_t^{(i)}\}$ satisfies the KKT conditions of (19).

C. Rectifier PWL Model Parameters

Table V lists the parameters of the concave PWL rectifier model $f(\cdot)$ in (13), obtained as described in Section IV-A. Each segment k is given by $f(P_{\text{rf}}) = a_k P_{\text{rf}} + b_k$, where P_{rf} and f are in mW.

References

[1] W. C. Brown, "The history of power transmission by radio waves," *IEEE Trans. Microw. Theory Techn.*, vol. MTT-32, no. 9, pp. 1230–1242, Sep. 1984, doi: 10.1109/TMTT.1984.1132833.

[2] M. Zorzi, A. Gluhak, S. Lange, and A. Bassi, "From today's INTRAnet of things to a future Internet of Things: A wireless- and mobility-related view," *IEEE Wireless Commun.*, vol. 17, no. 6, pp. 44–51, Dec. 2010, doi: 10.1109/MWC.2010.5675777.

[3] B. Clerckx, R. Zhang, R. Schober, D. W. K. Ng, D. I. Kim, and H. V. Poor, "Fundamentals of wireless information and power transfer: From RF energy harvester models to signal and system designs," *IEEE J. Sel. Areas Commun.*, vol. 37, no. 1, pp. 4–33, Jan. 2019, doi: 10.1109/JSAC.2018.2872615.

[4] X. Lu, D. Niyato, P. Wang, D. In Kim, and Z. Han, "Wireless charger networking for mobile devices: Fundamentals, standards, and applications," *IEEE Wireless Commun.*, vol. 22, no. 2, pp. 126–135, Apr. 2015, doi: 10.1109/MWC.2015.7096295.

[5] X. Liu, "Qi standard wireless power transfer technology development toward spatial freedom," *IEEE Circuits Syst. Mag.*, vol. 15, no. 2, pp. 32–39, 2nd Quart., 2015, doi: 10.1109/MCAS.2015.2419011.

[6] M. Budhia, G. Covic, and J. Boys, "A new IPT magnetic coupler for electric vehicle charging systems," in *Proc. 36th Annu. Conf. IEEE Ind. Electron. Soc.*, Nov. 2010, pp. 2487–2492, doi: 10.1109/IECON.2010.5675350.

[7] A. Kurs, A. Karalis, R. Moffatt, J. D. Joannopoulos, P. Fisher, and M. Soljačić, "Wireless power transfer via strongly coupled magnetic resonances," *Science*, vol. 317, no. 5834, pp. 83–86, Jul. 2007, doi: 10.1126/science.1143254.

[8] W. C. Brown, "The technology and application of free-space power transmission by microwave beam," *Proc. IEEE*, vol. 62, no. 1, pp. 11–25, Jan. 1974, doi: 10.1109/PROC.1974.9380.

[9] B. Strassner and K. Chang, "Microwave power transmission: Historical milestones and system components," *Proc. IEEE*, vol. 101, no. 6, pp. 1379–1396, Jun. 2013, doi: 10.1109/JPROC.2013.2246132.

[10] N. Tesla, "*System of electrical distribution*," U.S. Patent 381 970, May 1, 1888.

[11] Y. Zhang and B. Clerckx, "Waveform design for wireless power transfer with power amplifier and energy harvester non-linearities," *IEEE Trans. Signal Process.*, vol. 71, pp. 2638–2653, 2023, doi: 10.1109/TSP.2023.3278374.

[12] A. Azarbahram, O. L. A. López, and M. Latva-Aho, "Waveform optimization and beam focusing for near-field wireless power transfer with dynamic metasurface antennas and non-linear energy harvesters," *IEEE Trans. Wireless Commun.*, vol. 24, no. 2, pp. 1031–1045, Feb. 2025, doi: 10.1109/TWC.2024.3503908.

[13] A. B. Khattak, A. Azarbahram, D. Kumar, M. Latva-Aho, and O. L. A. López, "End-to-end joint waveform and beamforming optimization for RF wireless power transfer with hybrid transmit architecture and nonlinear energy harvesters," *IEEE Internet Things J.*, vol. 13, no. 6, pp. 10196–10212, Mar. 2026, doi: 10.1109/JIOT.2025.3631508.

[14] H. T. Friis, "A note on a simple transmission formula," *Proc. IRE*, vol. 34, no. 5, pp. 254–256, May 1946, doi: 10.1109/jrproc.1946.234568.

[15] J.-H. Kim, Y. Lim, and S. Nam, "Efficiency bound of radiative wireless power transmission using practical antennas," *IEEE Trans. Antennas Propag.*, vol. 67, no. 8, pp. 5750–5755, Aug. 2019, doi: 10.1109/TAP.2019.2922444.

[16] H. Y. Kim, Y. Lee, and S. Nam, "Efficiency bound estimation for a practical microwave and mmWave wireless power transfer system design," *J. Electromagn. Eng. Sci.*, vol. 23, no. 1, pp. 69–74, Jan. 2023, doi: 10.26866/jees.2023.1.r.146.

[17] S. Kojima, T. Mitani, and N. Shinohara, "Array optimization for maximum beam collection efficiency to an arbitrary receiving plane in the near field," *IEEE Open J. Antennas Propag.*, vol. 2, pp. 95–103, 2021, doi: 10.1109/OJAP.2020.3044443.

[18] S. Prasad, "On the index for array optimization and the discrete prolate spheroidal functions," *IEEE Trans. Antennas Propag.*, vol. AP-30, no. 5, pp. 1021–1023, Sep. 1982, doi: 10.1109/TAP.1982.1142900.

[19] G. Oliveri, L. Poli, and A. Massa, "Maximum efficiency beam synthesis of radiating planar arrays for wireless power transmission," *IEEE Trans. Antennas Propag.*, vol. 61, no. 5, pp. 2490–2499, May 2013, doi: 10.1109/TAP.2013.2241714.

[20] X. Yang, W. Geyi, and H. Sun, "Optimum design of wireless power transmission system using microstrip patch antenna arrays," *IEEE Antennas Wireless Propag. Lett.*, vol. 16, pp. 1824–1827, 2017, doi: 10.1109/LAWP.2017.2682262.

[21] Y.-S. Lee, J. Oh, and S. Nam, "An effect of time reversal based multiple beacon selection on wireless power transfer performance," in *Proc. Int. Symp. Antennas Propag. (ISAP)*, Nov. 2024, pp. 1–2, doi: 10.1109/ISAP62502.2024.10846697.

[22] J. Xu and R. Zhang, "A general design framework for MIMO wireless energy transfer with limited feedback," *IEEE Trans. Signal Process.*, vol. 64, no. 10, pp. 2475–2488, May 2016, doi: 10.1109/TSP.2016.2526965.

[23] Y.-S. Lee, J. Oh, and S. Nam, "Effects of magnitude dynamic range constraints on MIMO wireless power transfer efficiency," in *Proc. Int. Symp. Antennas Propag. (ISAP)*, Oct. 2025, pp. 1–2, doi: 10.23919/ISAP63122.2025.11361879.

[24] A. Hajimiri, B. Abiri, F. Bohn, M. Gal-Katziri, and M. H. Manohara, "Dynamic focusing of large arrays for wireless power transfer and beyond," *IEEE J. Solid-State Circuits*, vol. 56, no. 7, pp. 2077–2101, Jul. 2021, doi: 10.1109/JSSC.2020.3036895.

[25] Y.-S. Lee, J. Oh, and S. Nam, "Sequential feedback-based phase optimization using Hadamard basis for wireless power transfer," in *Proc. IEEE Wireless Power Technol. Conf. Expo* (WPTCE), Italy, Jun. 2025, pp. 1–5, doi: 10.1109/WPTCE62521.2025.11062191.

[26] T. Yoon et al., "Overcoming efficiency degradation in wireless power transfer systems: A supply voltage modulation method empowered by 5.64-GHz 256-element antenna array receiving 10.6-watt," in *IEEE MTT-S Int. Microw. Symp. Dig.*, Jun. 2025, pp. 85–88, doi: 10.1109/IMS40360.2025.11104047.

[27] R. Zhang and C. K. Ho, "MIMO broadcasting for simultaneous wireless information and power transfer," *IEEE Trans. Wireless Commun.*, vol. 12, no. 5, pp. 1989–2001, May 2013, doi: 10.1109/TWC.2013.031813.120224.

[28] S. Wan and K. Huang, "Methods for improving the transmission-conversion efficiency from transmitting antenna to rectenna array in microwave power transmission," *IEEE Antennas Wireless Propag. Lett.*, vol. 17, no. 4, pp. 538–542, Apr. 2018, doi: 10.1109/LAWP.2018.2801320.

[29] H. Sun, S. Zhu, R. Ren, H. Zhang, and X. Ma, "Optimization of wireless power transmission under nonuniform incident power density distribution," *IEEE Antennas Wireless Propag. Lett.*, vol. 23, no. 1, pp. 39–43, Jan. 2024, doi: 10.1109/LAWP.2023.3316163.

[30] S. Shen and B. Clerckx, "Beamforming optimization for MIMO wireless power transfer with nonlinear energy harvesting: RF combining versus DC combining," *IEEE Trans. Wireless Commun.*, vol. 20, no. 1, pp. 199–213, Jan. 2021, doi: 10.1109/TWC.2020.3024064.

[31] Y.-S. Lee, T. Yoon, Y. J. Song, S. K. Hong, J. Oh, and S. Nam, "Transmission-conversion efficiency maximization technique for MIMO wireless power transfer systems in ISAC applications," *IEEE Antennas Wireless Propag. Lett.*, vol. 24, no. 11, pp. 4492–4496, Nov. 2025, doi: 10.1109/LAWP.2025.3578089.

[32] B. Yang, X. Chen, J. Chu, T. Mitani, and N. Shinohara, "A 5.8-GHz phased array system using power-variable phase-controlled magnetrons for wireless power transfer," *IEEE Trans. Microw. Theory Techn.*, vol. 68, no. 11, pp. 4951–4959, Nov. 2020, doi: 10.1109/TMTT.2020.3007187.

[33] Q. Hui, K. Jin, and X. Zhu, "Directional radiation technique for maximum receiving power in microwave power transmission system," *IEEE Trans. Ind. Electron.*, vol. 67, no. 8, pp. 6376–6386, Aug. 2020, doi: 10.1109/TIE.2019.2941150.

[34] B. Jiang, P. Li, S. Zheng, Y. Lin, and H. Xu, "A 24-GHz beam-steerable multinode wireless power transfer system with a maximum DC output of 5.7 dBm at 1-m distance," *IEEE Trans. Microw. Theory Techn.*, vol. 72, no. 11, pp. 6774–6789, Nov. 2024, doi: 10.1109/TMTT.2024.3402067.

[35] A. B. Khattak, O. L. A. López, A. Azarbahram, D. Kumar, and M. Latva-Aho, "End-to-end waveform and beamforming optimization for RF wireless power transfer," in *Proc. IEEE 25th Int. Workshop Signal Process. Adv. Wireless Commun. (SPAWC)*, Sep. 2024, pp. 516–520, doi: 10.1109/SPAWC60668.2024.10694404.

[36] Z.-Q. Luo, W.-K. Ma, A. M. So, Y. Ye, and S. Zhang, "Semidefinite relaxation of quadratic optimization problems," *IEEE Signal Process. Mag.*, vol. 27, no. 3, pp. 20–34, May 2010, doi: 10.1109/MSP.2010.936019.

[37] G. Scutari, F. Facchinei, P. Song, D. P. Palomar, and J.-S. Pang, "Decomposition by partial linearization: Parallel optimization of multi-agent systems," *IEEE Trans. Signal Process.*, vol. 62, no. 3, pp. 641–656, Feb. 2014, doi: 10.1109/TSP.2013.2293126.

[38] Y.-S. Lee et al., "LUT-based transmit mode calibration complexity reduction method for wireless power transfer," in *Proc. IEEE Wireless Power Technol. Conf. Expo (WPTCE)*, May 2024, pp. 137–141, doi: 10.1109/WPTCE59894.2024.10557392.

[39] Y.-S. Lee, T. Yoon, J. Oh, and S. Nam, "Design and calibration of a CW time reversal wireless power transfer transmitter with pilot signal detection," in *Proc. Asia–Pacific Microw. Conf. (APMC)*, Dec. 2025, pp. 1–3, doi: 10.1109/APMC65046.2025.11378159.

[40] Y.-S. Lee et al., "A design and characterization method of a scalable large transmitting array for wireless power transfer," *IEEE Trans. Microw. Theory Techn.*, vol. 73, no. 6, pp. 3346–3358, Jun. 2025, doi: 10.1109/TMTT.2024.3487911.

[41] Y.-S. Lee, T. Yoon, J. Oh, and S. Nam, "DC-to-DC efficiency maximization in wireless power transfer with PA and rectifier nonlinearities via semidefinite relaxation," in *Proc. IEEE Wireless Power Technol. Conf. Expo (WPTCE)*, Halifax, NS, Canada, Jul. 2026, pp. 1–6.

[42] Skyworks Solutions, Inc. *SE5004L: 5 GHz, 26 dBm Power Amplifier With Power Detector.*. Accessed: Jul. 22, 2026. [Online]. Available: https://www.skyworksinc.com/-/media/skyworks/documents/products/601-700/se5004l_202393b.pdf

[43] Skyworks Solutions, Inc. *SE5004L-EK1: 802.11a/n 26 dBm WLAN RF Power Amplifier Evaluation Kit.*. Accessed: Jul. 22, 2026. [Online]. Available: https://www.cdiweb.com/datasheets/skyworks/se5004l-ek1_202643a.pdf

[44] T. Yoon et al., "Hardware-aware MILP for optimal end-to-end efficiency in MISO WPT: Joint optimization of power modes and fault tolerance," *IEEE Trans. Microw. Theory Tech.* accepted.

[45] S.-H. Li, J. Zhang, and S. S. H. Hsu, "A sub-6 GHz ultra-compact 69.8% drain efficiency harmonic control Doherty power amplifier in GAN technology," in *IEEE MTT-S Int. Microw. Symp. Dig.*, Jun. 2025, pp. 647–650, doi: 10.1109/IMS40360.2025.11103991.

[46] K. Dang et al., "A 5.8-GHz high-power and high-efficiency rectifier circuit with lateral GaN Schottky diode for wireless power transfer," *IEEE Trans. Power Electron.*, vol. 35, no. 3, pp. 2247–2252, Mar. 2020, doi: 10.1109/TPEL.2019.2938769.

[47] M. Razaviyayn, M. Hong, and Z.-Q. Luo, "A unified convergence analysis of block successive minimization methods for nonsmooth optimization," *SIAM J. Optim.*, vol. 23, no. 2, pp. 1126–1153, Jan. 2013, doi: 10.1137/120891009.

Young-Seok Lee (Graduate Student Member, IEEE) received the B.S. degree in electrical engineering from Korea University, Seoul, South Korea, in 2021, and the M.S. degree in electrical and computer engineering from Seoul National University, Seoul, in 2023, where he is currently pursuing the Ph.D. degree.

His research interests include wireless power transfer systems, optimization algorithms, antenna array calibration, target detection, and indoor localization.

Mr. Lee was a recipient of the Best Paper Award (Second Prize) at the 2024 International Symposium on Antennas and Propagation (ISAP 2024), in November 2024, the Best Paper Award (First Place) at the 2025 Winter Conference of the Korean Institute of Electromagnetic Engineering and Science (KIEES), in February 2025, and the Best Student Paper Award (Sole Recipient, First Place) at the 2026 IEEE Wireless Power Technology Conference and Expo (WPTCE 2026), in July 2026.

Taeyeong Yoon (Graduate Student Member, IEEE) received the B.S. degree (summa cum laude) in electronic engineering from Korea Aerospace University, Goyang, South Korea, in 2021, and the M.S. degree from the Department of Electrical and Computer Engineering, Seoul National University, Seoul, South Korea, in 2023, where he is currently pursuing the Ph.D. degree.

His current research interests include suppressing dual-polarized multipath coupling, dual-polarized antennas for sub-6-GHz applications, high-efficiency power amplifiers for millimeter-wave (mm-wave) applications, and RF/mm-wave/microwave integrated circuits.

Jungsuek Oh (Senior Member, IEEE) received the B.S. and M.S. degrees from Seoul National University, Seoul, South Korea, in 2002 and 2007, respectively, and the Ph.D. degree from the University of Michigan, Ann Arbor, MI, USA, in 2012.

From 2007 to 2008, he was a Hardware Research Engineer with Korea Telecom, Seoul, working on the development of flexible RF devices. In 2012, he was a Post-Doctoral Research Fellow with the Radiation Laboratory, University of Michigan. From 2013 to 2014, he was a Staff RF Engineer with Samsung Research America, Dallas, TX, USA, working as the Project Leader of the 5G/millimeter-wave antenna system. From 2015 to 2018, he was a Faculty Member with the Department of Electronic Engineering, Inha University, Incheon, South Korea. He is currently a Full Professor with tenure at the School of Electrical and Computer Engineering, Seoul National University, Seoul, South Korea. He has published more than 200 technical journal articles and conference papers. His research areas include mmWave beam focusing/shaping techniques, antenna miniaturization for integrated systems, radio propagation modeling for complex environments, and AI-based RF/EM system simulators.

Dr. Oh was a recipient of the 2011 Rackham Predoctoral Fellowship Award from the University of Michigan. His group has been recognized with numerous awards at leading academic and industrial conferences. He has served as a TPC Member and the Session Chair for the IEEE AP-S/USNC-URSI, ISAP, and APMC.

Sangwook Nam (Life Senior Member, IEEE) received the B.S. degree in electrical engineering from Seoul National University, Seoul, South Korea, in 1981, the M.S. degree in electrical engineering from Korea Advanced Institute of Science and Technology (KAIST), Seoul, in 1983, and the Ph.D. degree in electrical engineering from The University of Texas at Austin, Austin, TX, USA, in 1989.

From 1983 to 1986, he was a Researcher with the Gold Star Central Research Laboratory, Seoul. From 1990 to 2024, he was a Professor with the Department of Electrical and Computer Engineering, Seoul National University. He became an IEEE Life Senior Member in 2024. His research interests include the analysis and design of electromagnetic (EM) structures, antennas, microwave active/passive circuits, wireless power transfer, and radar systems.